

This is the peer reviewed version of the following article:

Wculek SK, Heras-Murillo I, Mastrangelo A, Mañanes D, Galán M, Miguel V, Curtabbi A, Barbas C, Chandel NS, Enríquez JA, Lamas S, Sancho D. Oxidative phosphorylation selectively orchestrates tissue macrophage homeostasis. *Immunity*. 2023 Mar 14;56(3):516-530.e9. doi: 10.1016/j.immuni.2023.01.011. Epub 2023 Feb 3. PMID: 36738738..

which has been published in final form at: <https://doi.org/10.1016/j.immuni.2023.01.011>

1 **Title: Oxidative phosphorylation selectively orchestrates tissue macrophage**
2 **homeostasis**

3 **Authors:** Stefanie K. Wculek^{1,*}, Ignacio Heras-Murillo¹, Annalaura Mastrangelo¹, Diego
4 Mañanes¹, Miguel Galán¹, Verónica Miguel², Andrea Curtabbi¹, Coral Barbas³, Navdeep S.
5 Chandel⁴, José Antonio Enríquez¹, Santiago Lamas², David Sancho^{1,5,*}

6 **Affiliations:**

7 ¹Centro Nacional de Investigaciones Cardiovasculares Carlos III (CNIC); Madrid, Spain

8 ²Program of Physiological and Pathological Processes, Centro de Biología Molecular
9 "Severo Ochoa" (CBMSO, CSIC-UAM); Madrid, Spain

10 ³Centro de Metabolómica y Bioanálisis (CEMBIO), Facultad de Farmacia, Universidad San
11 Pablo-CEU; Madrid, Spain

12 ⁴Department of Medicine, Northwestern University Feinberg School of Medicine; Chicago,
13 IL, USA

14 ⁵Lead contact

15 *Corresponding authors. Email: stefanie.wculek@cnic.es; dsancho@cnic.es

16 **Summary**

17 In vitro studies associated oxidative phosphorylation (OXPHOS) with anti-inflammatory
18 macrophages, while pro-inflammatory macrophages rely on glycolysis. However, the metabolic
19 needs of macrophages in tissues (TMFs) to fulfil their homeostatic activities are incompletely
20 understood. Here, we identified OXPHOS as the highest discriminating process among TMFs from
21 different organs in homeostasis by analysis of RNAseq data, in both human and mouse. Impairing
22 OXPHOS in TMFs via *Tfam* deletion differentially affected TMF populations. *Tfam* deletion
23 resulted in reduction of alveolar macrophages (AMs) due to impaired lipid-handling capacity,
24 leading to increased cholesterol content and cellular stress, causing cell cycle arrest in vivo. In
25 obesity, *Tfam* depletion selectively ablated pro-inflammatory lipid-handling white adipose tissue
26 macrophages (WAT-MFs), preventing insulin resistance and hepatosteatosis. Thus, OXPHOS,
27 rather than glycolysis, distinguishes TMF populations and is critical for the maintenance of TMFs
28 with a high lipid-handling activity, including pro-inflammatory WAT-MFs. This could provide a
29 selective therapeutic targeting tool.

30 **Keywords**

31 Tissue macrophages, Immunometabolism, Oxidative phosphorylation, *Tfam*, Cholesterol
32 handling, Obesity, Proinflammatory macrophages

33 **Introduction**

34 Macrophages originate from embryonic progenitors or incoming monocytes and colonize the
35 majority of organs in the body. Those macrophages in tissues (TMFs) not only contribute to innate
36 immunity, but perform distinct activities to maintain local and systemic homeostasis in the
37 complex environment of tissues (Nobs and Kopf, 2021). For instance, alveolar macrophages
38 (AMs) remove excess surfactant for optimal gas exchange in the lung, splenic red pulp
39 macrophages (RPMs), and hepatic Kupffer cells (KCs) recycle iron from erythrocytes and
40 facilitate lipid homeostasis, while lean white adipose tissue macrophages (WAT-MFs) aid
41 adipogenesis and thermogenesis (Nobs and Kopf, 2021; Remmerie and Scott, 2018; Schneider et
42 al., 2014; Wculek et al., 2022).

43 The emerging field of immunometabolism is uncovering the relationship between metabolic
44 features and functionality of immune cells, including macrophages. Cells adapt the use of
45 metabolites derived from sugars, amino acids or lipids for either anabolic or catabolic purposes,
46 for energy production or synthesis of cellular components, respectively. The main bioenergetic
47 processes in eukaryotic cells are lactate production following glycolysis in the cytosol and
48 oxidative phosphorylation (OXPHOS) in the mitochondria. This mitochondrial respiration can be
49 fueled by the degradation of various nutrients beyond glucose that enter the TCA cycle, such as
50 glutaminolysis or fatty acid (FA) oxidation (O'Neill et al., 2016). In vitro, exposure to specific
51 stimuli induces metabolic reprogramming of bone marrow-derived macrophages (BMDMs) that
52 underlies their activities. Enhanced glycolysis and a broken tricarboxylic acid (TCA) cycle are
53 associated with pro-inflammatory M1 macrophage polarization, while anti-inflammatory M2
54 macrophages are characterized by glutamine and FA-fueled mitochondrial respiration (Faas et al.,
55 2021; Lauterbach et al., 2019; Russell et al., 2019). However, TMFs are metabolically plastic cells
56 that can distinctly tailor their cellular metabolism to facilitate their immune-promoting or resolving
57 functions. For example, large peritoneal macrophages (LPMs) use a glutamate-driven
58 mitochondrial metabolism for adequate microbial killing (Davies et al., 2017), yet AMs rely on
59 glycolysis for proper induction of type 2 inflammatory responses (Svedberg et al., 2019), but not
60 bacterial-induced inflammation (Woods et al., 2020), and the inflammation-resolving function of
61 cardiac macrophages requires FA oxidation and mitochondrial respiration (Zhang et al., 2019).
62 Nevertheless, the specific metabolic requirements for maintenance of TMF populations and their
63 functions in vivo during homeostasis are largely unknown (Caputa et al., 2019; Wculek et al.,
64 2022).

65 Moreover, non-infectious pathologic conditions can alter the tissue microenvironment and impact
66 TMFs metabolism and function (Nobs and Kopf, 2021; Wculek et al., 2022; Yang et al., 2020).
67 For instance, hypertrophy of WAT upon overnutrition causes excess lipid-load and adipocyte death
68 in obese individuals. This causes the adoption of an inflammatory state by a population of obese
69 WAT-MFs that subsequently contribute to the development of metabolic syndrome, insulin
70 resistance and lipid accumulation in the liver (Korf et al., 2019; Lefere and Tacke, 2019). Notably,
71 this pathologic functional change of obese WAT-MFs is accompanied by a profound metabolic
72 remodeling and bioenergetic activation (Boutens et al., 2018; Dahik et al., 2020; Hill et al., 2018;
73 Serbulea et al., 2018). Hence, understanding potentially distinct metabolic features of TMFs and
74 the effect on their function can uncover specific vulnerabilities of disease-promoting TMFs.

75 Here, we uncovered OXPHOS as the biological pathway that most differs at the transcriptional
76 level when comparing TMFs from different organs in homeostasis, both in human and mice. We
77 revealed a distinct homeostatic function-dependent susceptibility of TMFs in 8 organs to genetic
78 interference with mitochondrial respiration in mice. This vulnerability is determined by a high

79 extracellular cholesterol/lipid handling activity of specific TMF populations and could be rescued
80 by ex vivo culture or simvastatin treatment in vivo. Pro-inflammatory lipid-exposed WAT-MFs in
81 obesity also became sensitive to OXPHOS impairment, which ameliorated overnutrition-
82 associated pathologies. Collectively, our study demonstrates the diversity of the energy
83 metabolism of homeostatic TMF populations and uncovers a function-dependent metabolic
84 vulnerability of selected TMFs that can be exploited for therapeutic purposes.

85 **Results**

86 *Expression of OXPHOS-related genes is a main distinctive characteristic of both human and*
87 *mouse tissue macrophage populations in homeostasis*

88 To identify differences among TMF populations from different organs in homeostasis, we
89 interrogated publicly available single cell RNA sequencing (RNAseq) data of human organs from
90 the Human Cell Landscape database (Han et al., 2020). Firstly, pre-identified TMF clusters of the
91 10 organs containing sufficient macrophage numbers were aggregated by their origin to build
92 pseudo-bulk samples. Then, we performed a principal component analysis (PCA) and found that
93 TMFs from different organs clustered depending on their location (Figures 1A, 1B and S1A-S1D).
94 To identify which biological processes explained the differences in gene expression between
95 TMFs that was detected by the PCA, we performed a gene set-enrichment analysis of the genes
96 defining PC1 and PC2 loading vectors. This analysis identified OXPHOS-related pathways as the
97 main source of variance that separates human TMFs among each other depending on their organ
98 location (Figures 1C, 1D and S1E- S1H). Next, we performed a similar PCA-based gene set-
99 enrichment analysis on bulk RNAseq data of 10 mouse TMF populations from healthy mice from
100 the Immunological Genome Project (Yoshida et al., 2019). This analysis revealed a location-
101 dependent clustering of TMFs and OXPHOS as a distinguishing biological process also when
102 comparing mouse TMF populations located in different organs with each other (Figures 1E-1G
103 and S2A-S2E). OXPHOS is the main catabolic and cellular energy-producing pathway in
104 eukaryotic cells (Russell et al., 2019). The oxidation of nutrients in the tricarboxylic acid (TCA)
105 cycle in mitochondria allows electrons to enter the electron transport chain (ETC) via complex I
106 or complex II and their transport through complex III and IV generates a proton gradient across
107 the inner mitochondrial membrane. This membrane potential drives ATP generation by the ATP
108 synthase as final step of mitochondrial respiration and OXPHOS. Mitochondria harbor their own
109 genome that encodes several proteins of the ETC complexes (Baixauli et al., 2015; Desdín-Micó
110 et al., 2020; Latorre-Pellicer et al., 2019; Smeitink et al., 2001). Notably, mitochondrially encoded
111 (mt-) genes displayed the highest log-Fold changes of OXPHOS-related genes among distinct
112 mouse TMF populations (Figures 1H and S2E). This finding indicates that a distinct catabolic
113 OXPHOS metabolism distinguishes TMFs in homeostasis from each other based on their organ
114 location, in both mouse and human.

115 *OXPHOS targeting differentially impacts tissue macrophages in the steady state*

116 To study the relevance of mitochondrial respiration in TMF function in vivo, we deleted the
117 mitochondrial transcription factor A (*Tfam*) in TMF populations by crossing *Tfam*^{fl/fl} mice with
118 *CD11c*^{Cre} (*CD11cΔTfam*) or *Lyz2*^{Cre} (*LysMΔTfam*) mice. *Tfam* is nuclear-encoded and follows a
119 similar expression pattern in mouse TMFs as mt-genes (Figure S2F). *Tfam* controls the replication
120 and transcription of mt-DNA and mt-encoded genes that include components of complex I, III, IV
121 and V of the ETC. Hence, *Tfam* depletion simultaneously targets several ETC complexes that
122 underlie functional OXPHOS and *Tfam* loss was previously shown to strongly reduce

123 mitochondrial respiration in different immune cell subsets (Baixauli et al., 2015; Desdín-Micó et
124 al., 2020; Gao et al., 2022; Larsson et al., 1998; Smeitink et al., 2001). By using distinct
125 macrophage-targeting Cre drivers, we achieved *Tfam* mRNA deletion (Figure 2A) and
126 consequently depletion of mt-DNA (Figure 2B), a functional readout for *Tfam* loss which underlies
127 OXPHOS impairment, in several different TMFs. Notably, *Tfam* deletion largely reduced the
128 numbers of AMs, LPMs, Langerhans cells (LCs), KCs and RPMs, while kidney macrophages
129 (KMs) or lean inguinal and epididymal WAT-MFs (iWAT-MFs or eWAT-MFs) numbers were
130 unaltered (Figures 2C and 2D). Reduction in numbers of the TMF populations significantly
131 correlated with their expression of mt-genes (Figures 1H, 2C and 2E), the latter being an indication
132 for their mitochondrial activity. Moreover, TMFs that are more sensitive to OXPHOS-interference
133 also increased their levels of autofluorescence (Figure 2F), which is often a sign of phenotypic
134 alterations in macrophages. Overall, our data identify OXPHOS as a distinguishing feature
135 between TMF populations with functional relevance for maintenance of specific TMF populations.

136 *OXPHOS-impaired alveolar macrophages undergo cell cycle arrest and apoptosis despite normal*
137 *ATP levels*

138 To understand the reasons behind the distinct use of OXPHOS by homeostatic TMFs in different
139 organs, we further analyzed AMs, which are profoundly depleted upon OXPHOS interference
140 (Figure 2C). Initial colonization of the lung by control *Tfam^{fl/fl}* and *CD11cΔTfam* AMs at postnatal
141 day 2 and 11 was comparable, however *Tfam*-deficient AM numbers started declining 3 weeks
142 after birth (Figures 3A and S3A). Phenotypic alterations of *CD11cΔTfam* AMs also appeared
143 progressively, such as the deregulation of Siglec F and CD11b, indicative of impaired maturation,
144 as well as autofluorescence, cell size and forward and side scatter profiles (FSC and SSC) (Figures
145 3B, 3C, S3B and S3C). A similar reduction in AM presence and maturity was confirmed in
146 *LysMΔTfam* mice, an alternative Cre-line to target AMs, compared with their control littermates
147 (Figure S3D). In line with the progressive reduction of AM numbers, *CD11cΔTfam* mice
148 developed pulmonary alveolar proteinosis (PAP), that worsened over time. PAP was demonstrated
149 by presence of protein, debris, dead cells and immune cell infiltrates in the bronchoalveolar lavage
150 (BAL) (Figures 3D and S3E). Notably, *Tfam* deficiency caused a decreased proliferation and an
151 increased apoptosis of AMs, especially in 3 week-old mice (Figures 2E, 2F and S3F), which
152 explains the decline of the population.

153 *CD11cΔTfam* AMs displayed decreased respiratory rates (Figures 3G and S3G), a slight reduction
154 in mitochondrial content (Figure S3H) and a lower mitochondrial membrane potential (Figures 3H
155 and S3I) compared with *Tfam^{fl/fl}* littermates. Consistently, *Tfam* targeting in AMs showed a mild
156 functional impairment of OXPHOS. This is likely explained by the fact that *Tfam* is the upstream
157 factor that controls transcription of mt-encoded components of ETC complexes along with the
158 accumulation of ETC complexes before Cre expression. Importantly, the partial effect in OXPHOS
159 offers the advantage to study the modulation of OXPHOS activity in *CD11cΔTfam* AMs rather
160 than a complete loss of mitochondria or their function, which could be more artefactual and
161 aggressive. We next explored whether a bioenergetic deficiency could explain the limited
162 maintenance of AMs upon *Tfam* loss. However, total ATP levels were equal in *Tfam^{fl/fl}* and
163 *CD11cΔTfam* AMs (Figures 3I and S3J), despite lower production of mitochondrial ATP (Figure
164 S3G). Notably, ATP levels of *Tfam*-deficient, but not control, AMs were sensitive to the glycolysis
165 inhibitor 2-deoxy-D-glucose (Figure 3I). *Tfam*-deficient AMs also secreted more lactate (Figure
166 3J) and showed a higher extracellular acidification rate (Figure 3K). These results indicate a
167 rewiring of the central carbon metabolism and bioenergetics towards lactic fermentation by

168 *CD11cΔTfam* AMs to prevent an energetic crisis. Nevertheless, OXPHOS impairment upon *Tfam*-
169 deficiency causes apoptosis and reduces proliferation of AMs.

170 *A deregulated TCA cycle associates with impaired numbers and phenotype of ETC-deficient*
171 *alveolar macrophages*

172 To dissect the underlying bioenergetics-independent mechanisms causing the decline of the AM
173 population upon OXPHOS interference, we performed an RNAseq analysis of AMs from 3 week-
174 old *CD11cΔTfam* and control mice as well as GC/MS metabolomics of adult AMs (Figures S4A-
175 C). The transcriptomic analysis confirmed a reduction of OXPHOS and deregulated cell
176 proliferation as well as apoptosis in *Tfam*-deficient AMs (Figures S2B and S4D-F). Metabolically,
177 glucose and its derivatives were more abundant in *CD11cΔTfam* than *Tfam^{fl}* AMs together with
178 the upregulation of genes involved in glucose uptake and metabolism, such as *Slc2a1* (Figures
179 S4G-I), which is in line with enhanced glycolysis. Notably, we observed a profound deregulation
180 of expression of genes regulating the TCA cycle and amino acid metabolism as well as enhanced
181 levels of TCA cycle metabolites and glucogenic amino acids in *Tfam*-deficient AMs (Figures 3L,
182 3M, S4J and S4K). Individual TCA cycle metabolites play distinct roles in cellular metabolism,
183 for example fumarate causes hypoxia-inducible factor 1 α stabilization and reactive oxygen species
184 (ROS) signaling (Martínez-Reyes and Chandel, 2020). However, the global deregulation of
185 numerous TCA cycle-associated enzymes and intermediates, as well as of TCA cycle-fueling
186 metabolites such as amino acids, points towards a broad adaption of cellular catabolic metabolism
187 in *Tfam*-deficient AMs. All catabolic processes in eukaryotic cells converge into the TCA cycle
188 and its functioning is closely intertwined with mitochondrial OXPHOS. Complex III and IV are
189 always required for the functioning of the ETC, while electrons may enter the ETC either via
190 complex I or complex II (Martínez-Reyes and Chandel, 2020). Importantly, the ETC complex II
191 is also known as succinate dehydrogenase (SDH) and an enzyme within the TCA cycle, whereas
192 complex I, III and IV only participate in the ETC and OXPHOS (Martínez-Reyes and Chandel,
193 2020). Nevertheless, a deficiency of complex III also deregulates the TCA cycle and the abundance
194 of its metabolites (Weinberg et al., 2019). Hence, in order to understand the relevance of a TCA
195 cycle deregulation for the maintenance of *Tfam*-deficient AMs, we individually deleted
196 components of either complex I, II, III or IV in those cells. Firstly, *CD11cΔUqcrcq* (deficient in
197 *Uqcrcq*, mitochondrial complex III gene) and *CD11cΔCox10* (deficient in *Cox10*, mitochondrial
198 complex IV gene) mice displayed a reduction in numbers of AMs and an altered AM phenotype
199 compared with their control littermates (Figures 3N and 3O), reminiscent of the phenotype of
200 *CD11cΔTfam* AMs (Figures 3A-C). Moreover, *CD11cΔSdhb* (deficient in *Sdhb*, mitochondrial
201 complex II gene) mice also exhibited reduced AM numbers and an impaired AM phenotype
202 compared with their control littermates, similar to complex III and IV deficiency (Figures 3N and
203 3O). Of note, AM numbers were comparable in *CD11cΔNdufs4* (deficient in *Ndufs4*,
204 mitochondrial complex I gene whose deletion results in a complex I hypomorph) mice compared
205 with their controls (Figures 3N and 3O). The ETC complex I does not directly participate in the
206 TCA cycle, but oxidizes NADH to maintain a healthy NAD⁺/NADH ratio. However,
207 mitochondrial NADH oxidation also occurs during the folate pathway or through the activity of
208 the Nicotinamide Nucleotide Transhydrogenase, for instance, which potentially rescue this
209 function of complex I. Altogether, these results indicate the importance of the mitochondrial ETC
210 driven by complex II and, hence, the correct functioning of the TCA cycle for AM proliferation
211 and survival.

212 *Cellular stress and reduced proliferation in OXPHOS-impaired alveolar macrophages depend on*
213 *the tissue microenvironment*

214 As a potential molecular mechanism for induction of cell cycle arrest and apoptosis (Feng et al.,
215 2003; Yao et al., 2014), we detected induction of activating transcription factor 4 (*Atf4*) and
216 corresponding cellular stress-related genes in *Tfam*-deficient AMs (Figures 4A and 4B). ATF4 is
217 the effector of the integrated stress response (ISR) located downstream of the eukaryotic initiation
218 factor (eIF) 2 α . The ISR is induced upon different stress stimuli via activation of four distinct
219 known kinases that phosphorylate eIF2 α to re-establish cellular homeostasis (Pakos-Zebrucka et
220 al., 2016). Double-stranded RNA-dependent protein kinase (PKR) and general control non-
221 depressible protein (GCN) 2 were unlikely to be activated in *CD11c Δ Tfam* AMs. They usually
222 respond to stresses related with viral infection or amino acid deprivation, while *Tfam*-deficient
223 AMs were analyzed in homeostasis and harbored elevated amino acid levels compared with
224 controls (Figure S4K). The PKR-like ER kinase (PERK)/eIF2 α /ATF4 signaling pathway is
225 generally induced upon endoplasmic reticulum (ER) stress and can regulate the
226 immunosuppressive function of macrophages (Raines et al., 2022). However, ATF4 induces
227 apoptosis in situations of prolonged ER stress via activation of C/EBP homologous protein
228 (CHOP) (Nishitoh, 2012). In fact, the “intrinsic apoptotic signaling pathway in response to
229 endoplasmic reticulum stress” and expression of the gene encoding CHOP (*Ddit3*) was
230 significantly upregulated in AMs from 3 week-old *CD11c Δ Tfam* compared with control mice
231 (Figures 4A and S4B). We also detected increased splicing of X-box binding protein (*Xbp*) 1 in
232 those *CD11c Δ Tfam* AMs (Figure 4C), which is mediated by inositol-requiring enzyme (IRE) 1
233 upon ER stress independently of the PERK/eIF2 α /ATF4 axis, further indicating the induction of
234 ER stress in *Tfam*-deficient AMs. Moreover, *CD11c Δ Tfam* AMs displayed enhanced expression
235 of genes associated with mitochondrial stress compared with *Tfam*^{fl/fl} AMs (Figure S5A), which can
236 activate the ISR via heme-regulated eIF2 α kinase (HRI) (Fessler et al., 2020; Guo et al., 2020).
237 We also observed increased generation of ROS and signs of oxidative stress, such as activation of
238 genes involved in glutathione synthesis and arachidonic acid expression and release (Figures S5B-
239 D).

240 Given the tissue location-dependent effects of *Tfam* deletion in TMFs (Figure 2), we interrogated
241 potential microenvironmental cell-extrinsic causes of cellular stress in *CD11c Δ Tfam* AMs. To this
242 end, we harvested AMs from 3 week-old mice by BAL and cultured them for 48 hours. Notably,
243 ex vivo cultured *CD11c Δ Tfam* AMs normalized their *Atf4* expression levels to that of *Tfam*^{fl/fl} AMs
244 (Figure 4D). This rescue was accompanied by a recovery of the proliferative capacity and
245 expression of cell cycle and apoptotic genes in *Tfam*-deficient AMs (Figures 4E, 4F and S5E).
246 This finding indicated an environmental extrinsic trigger of cellular stress that interferes with the
247 maintenance of *Tfam*-deficient AMs. Oxidative or mitochondrial stress is unlikely to solely
248 account for the activation of the ISR in *CD11c Δ Tfam* AMs because this type of cellular stress is
249 most probably a result of the genetic interference with mitochondrial respiration upon *Tfam* loss
250 and therefore cell intrinsic. Notably, culturing of AMs under presence of PERK inhibition already
251 ameliorated the *Atf4* levels in *CD11c Δ Tfam* AMs after only 6 hours of culture (Figure S5F). This
252 PERK blockade-mediated acceleration of the ISR reduction upon ex vivo culture suggests the
253 involvement of ER stress in the induction of *Atf4* in *Tfam*-deficient AMs in vivo, likely additional
254 to *Tfam* loss-induced mitochondrial stress. In conclusion, the tissue microenvironment is inducing
255 the cellular/ER stress in *CD11c Δ Tfam* AMs that, in turn, causes their impaired proliferation.

256 *Altered extracellular lipid and cholesterol handling ability causes the loss of Tfam-deficient*
257 *alveolar macrophages in vivo*

258 In homeostasis, most AMs are located in the lung alveoli and exposed to pulmonary surfactant,
259 that is mainly composed of glycerophospholipids and cholesterol (Fessler and Summer, 2016).
260 The predominant function of AMs is the removal of the lipid-rich surfactant (Nobs and Kopf, 2021;
261 Wculek et al., 2022). The TCA cycle, which is deregulated in *Tfam*-deficient AMs (Figures 3L
262 and 3M), is vital for lipid and FA catabolism (Remmerie and Scott, 2018) and a deregulation of
263 cholesterol levels is a well-known inducer of ER stress in macrophages (Feng et al., 2003; Yao et
264 al., 2014). Hence, we hypothesized that a deregulated lipid handling capacity causes the reduced
265 proliferation and enhanced apoptosis in OXPHOS-impaired AMs. Indeed, *CD11cΔTfam* AMs
266 accumulated more intracellular lipids compared with *Tfam^{fl/fl}* AMs (Figures 5A and S6A). By
267 transmission electron microscopy, we observed large spiral-like structures in *Tfam*-deficient AMs,
268 which were absent from controls (Figure 5B). Those structures were highly reminiscent of
269 pulmonary surfactant (Botas et al., 1998) and the previously reported “cholesterol whorls” formed
270 by cholesterol-laden BMDMs in vitro (Tabas, 2002). Despite unaltered abundance of free FAs
271 (Figure S6B), *Tfam*-deficient AMs showed decreased oxidation of palmitate compared with
272 controls as well as a downregulation of genes involved in FA oxidation (Figures 5C and 5D). Lipid
273 catabolism, especially FA oxidation, the TCA cycle and OXPHOS are intricately linked processes.
274 FA oxidation generates Acyl-CoA that enters in the TCA cycle, but also delivers electrons directly
275 to the ETC and ubiquinone in the inner mitochondrial membrane forming ubiquinol. Re-oxidation
276 of ubiquinol is usually performed by complex III and IV, and interference with this process can
277 impair FA oxidation (Chokchaiwong et al., 2018). Hence, a defective OXPHOS metabolism
278 frequently results in reduced FA oxidation in macrophages (O’Neill et al., 2016; Remmerie and
279 Scott, 2018; Russell et al., 2019). In line, *Tfam*-deficient AMs also displayed a lower oxygen
280 consumption and respiratory rate in media containing only FA fuels (Figure S6C).

281 Notably, cholesterol was strongly enriched in *CD11cΔTfam* vs *Tfam^{fl/fl}* AMs. This could not be
282 ascribed to increased endogenous cholesterol biosynthesis as the controlling genes were even
283 downregulated. Rather, signatures for cholesterol uptake, transport and storage were strongly
284 deregulated and cholesterol efflux-related genes downregulated (Figures 5E, 5F and S6D). This
285 includes the downregulation of the ABC transporter gene *Abcg1*, which is vital for AM
286 functionality and cholesterol efflux (Thomassen et al., 2007). Notably, *Tfam*-deficient AMs
287 imported more and exported less cholesterol than control AMs (Figure 5G). The deregulated
288 expression of lipid/cholesterol handling-related genes and enhanced lipid accumulation occurred
289 already in AMs of 3 week-old *CD11cΔTfam* mice (Figures 5D, 5E, S6A and S6D), when no
290 elevation of cholesterol levels was detected in the BAL (Figure S6E). This suggests that the
291 increased intracellular lipid/cholesterol levels in *Tfam*-deficient AMs are a result of their inability
292 to process homeostatic amounts of lipids/cholesterol and not a reflection of elevated cholesterol
293 levels in the lung. The nuclear receptor transcription factors liver X receptors (LXR) α and β are
294 the master regulators of intracellular cholesterol handling (Remmerie and Scott, 2018). We found
295 that numerous LXR α/β target genes are deregulated in *CD11cΔTfam* vs *Tfam^{fl/fl}* AMs (Figure S6F).
296 Mitochondria are known to contribute to LXR activation. The mitochondrial proteins mitofusin 2
297 and optic atrophy 1, the mitochondrial inhibitor oligomycin, as well as mitochondria-derived ATP
298 can regulate cholesterol handling and efflux in macrophages (Graham, 2015; Karunakaran et al.,
299 2015). A current model for mitochondrial cholesterol transport involves a trafficking complex
300 containing steroidogenic acute regulatory (STAR) proteins that delivers cholesterol to the
301 mitochondrial enzyme sterol 27-hydroxylase (Cyp27a1). Cyp27a1 converts cholesterol into
302 endogenous LXR ligands (Fu et al., 2001; Graham, 2015). We found transcripts of STAR proteins

303 to be deregulated and *Cyp27a1* to be downregulated in *Tfam*-deficient AMs (Figures 5E and S6G).
304 Notably, *CD11cΔTfam* AMs remained equally responsive to LXR activation as *Tfam^{fl/fl}* AMs,
305 demonstrated by similar upregulation of the LXR target gene *Abcg1* upon treatment with LXR
306 ligands (Figure S6H). Hence, limited activation of LXR signaling, likely due to decreased
307 mitochondrial cholesterol transport and LXR ligand generation, and the reduced mitochondrial
308 ATP production (Figure S3G) mechanistically contribute to the defective cholesterol handling and
309 accumulation in *Tfam*-deficient AMs.

310 Elevated intracellular cholesterol levels can cause cellular/ER stress and ATF4 activation in
311 macrophages (Feng et al., 2003; Yao et al., 2014). To understand if lipids, mainly cholesterol, are
312 the extracellular factors driving the progressive decline of *Tfam*-deficient AMs, we aimed to
313 reduce those lipid levels in vivo. Simvastatin is a clinically approved cholesterol synthesis inhibitor
314 that reduces cholesterol levels in BAL as well as in AMs of mice with PAP and improves the
315 disease upon systemic administration (McCarthy et al., 2018). Treatment with simvastatin mildly
316 decreased systemic cholesterol and triglycerides in serum and total cholesterol levels in BAL of
317 *CD11cΔTfam* mice without ameliorating other readouts of PAP, such as BAL turbidity or protein
318 content (Figures 5H, S6I and S6J). Nevertheless, simvastatin treatment significantly increased the
319 numbers of *Tfam*-deficient AMs in the lung and enhanced their proliferation (Figures 5I and S6K).
320 While we cannot exclude a contribution of additional mechanisms, those findings indicate that the
321 inability of processing of extracellular lipids by *Tfam*-deficient AMs causes enhanced intracellular
322 levels of cholesterol and other lipids. This induces cellular/ER stress and ATF4 activation in AMs
323 and culminates in their apoptosis, reduced proliferation and progressive loss of the population in
324 vivo.

325 *High cholesterol handling activity determines the vulnerability of tissue macrophages to OXPHOS* 326 *impairment*

327 Next, we hypothesized that a similar mechanism could affect other TMF populations that are
328 vulnerable to OXPHOS interference. To address this, we investigated lipid handling and cellular
329 stress in selected TMFs whose presence is reduced upon *Tfam* deletion (Figure 2C). Similar to
330 AMs, numbers of LCs and RPMs were decreased by impairment of ETC complex II, III as well as
331 IV, while they remained unaltered by complex I dysfunction compared with control littermates
332 (Figure 6A). ATP content was unchanged in *Tfam*-deficient RPMs and LPMs, and both
333 accumulated more intracellular lipids and increased the expression of *Atf4* (Figures 6B-6D).
334 Notably, simvastatin treatment also enhanced the presence of RPMs in *CD11cΔTfam* mice (Figure
335 6E). Moreover, the expression of OXPHOS-related genes not only significantly correlated with
336 genes involved in lipid and FA catabolism, but especially cholesterol handling processes in human
337 and mouse TMFs (Figure 6F and 6G). Overall, our data suggests that OXPHOS dysfunction
338 selectively affects TMFs with high lipid/cholesterol processing activity by impairing their ability
339 to oxidize and efflux extracellular lipids. This results in cholesterol accumulation that drives
340 cellular/ER stress, cell cycle arrest and apoptosis of lipid-handling TMFs (Figure 6H).

341 *OXPHOS-impairment depletes pro-inflammatory, but not anti-inflammatory, eWAT-MFs and* 342 *ameliorates obesity-related pathologies*

343 We hypothesized that the alteration of the tissue microenvironment towards an increased lipid
344 content could enhance the vulnerability of TMFs to OXPHOS interference. We found that lean
345 WAT-MF populations, which are metabolically quiescent (Boutens et al., 2018; Serbulea et al.,
346 2018), are largely undisturbed by *Tfam* deletion in homeostasis (Figure 2). However, during

347 overnutrition-induced obesity, eWAT hypertrophy causes adipocyte death and the release of lipids
348 into the microenvironment. This triggers recruitment of monocyte-derived eWAT-MFs, that also
349 proliferate locally (Amano et al., 2014), form crown-like structures (CLS) around dying
350 adipocytes, become pro-inflammatory and participate in handling those excess extracellular lipids
351 (Hill et al., 2018; Li et al., 2010; Wculek et al., 2022; Yang et al., 2020). Hence, we reasoned that
352 OXPHOS impairment could selectively affect the maintenance and proliferation those pro-
353 inflammatory eWAT-MFs during obesity and fed *Tfam*^{ff} and *LysMΔTfam* mice with a high fat diet
354 (HFD). Notably, HFD-fed *LysMΔTfam* mice gained less fat mass than *Tfam*^{ff} animals, while their
355 lean mass was unaltered (Figures 7A and S7A). The tibiae length, food and drink intake, energy
356 expenditure, consumed O₂ volume as well as respiratory exchange ratio of obese *LysMΔTfam* mice
357 was similar to that of *Tfam*^{ff} controls, however the released CO₂ volume was increased (Figures
358 S7B-7D). In line with our hypothesis, pro-inflammatory CD11c⁺ and/or CD9⁺ eWAT-MFs
359 upregulated *Atf4* expression and reduced their proliferation upon *Tfam* deficiency, which resulted
360 in their reduced numbers (Figures 7B, 7C and S7E). Notably, similar to lean WAT-MFs, the
361 numbers, *Atf4* expression and proliferation of anti-inflammatory CD206⁺ and/or MerTK⁺ eWAT-
362 MFs remained unaltered in obese *LysMΔTfam* mice compared with *Tfam*^{ff} controls (Figures 7B,
363 7C and S7E). The largely unaltered expression of genes associated with anti-inflammatory
364 macrophage functions in eWAT (Figure S7F) supports this finding. This is likely due to a lower
365 lipid burden of those anti-inflammatory compared with pro-inflammatory CD11c⁺ and/or CD9⁺
366 eWAT-MFs, as the latter predominate in CLS (Hill et al., 2018; Li et al., 2010; Yang et al., 2020).
367 Of note, the numbers and phenotype of circulating monocytes, which can give rise to eWAT-MFs
368 in obesity, were unaffected in *LysMΔTfam* mice (Figure S7G). In accordance with decreased pro-
369 inflammatory eWAT-MF presence, obese *LysMΔTfam* mice displayed a lower number of CLS and
370 reduced inflammatory *Tnfa* and *Ccl2* cytokine levels in eWAT, but unaltered adipocyte size, as
371 well as lower systemic leukocyte numbers in plasma compared with *Tfam*^{ff} mice (Figures 7D-7F
372 and S7H). Moreover, the eWAT of HFD-fed *LysMΔTfam* mice displayed an elevated expression
373 of genes involved in lipid catabolism, lipolysis, ketogenesis and mitochondrial respiration than
374 that of *Tfam*^{ff} mice, but not lipogenesis (Figures 7G and 7H). This indicates a more metabolically
375 active state and a higher lipid oxidation in the eWAT (Bae et al., 2018), which appears independent
376 of eosinophil-mediated alternative macrophage activation and adipose tissue beigeing (Figures
377 S7F, S7I and S7J) (Rao et al., 2014). HFD-fed *LysMΔTfam* mice also showed higher glucose
378 tolerance and insulin sensitivity compared with *Tfam*^{ff} mice (Figure 7I and S7K). High-density
379 lipoprotein (LDL) and alanine aminotransferase (ALT) levels in plasma, liver weight as well as
380 hepatic lipid accumulation were also notably reduced in obese *LysMΔTfam* vs *Tfam*^{ff} mice (Figures
381 7J and S7L-O).

382 To corroborate those data, we next analyzed obese *CD11cΔUqcrcq* mice, where ETC complex III
383 and thereby OXPHOS dysfunction is limited to pro-inflammatory eWAT-MFs expressing CD11c.
384 HFD-fed *CD11cΔUqcrcq* mice gained less weight and harbored lower pro-inflammatory eWAT-
385 MF numbers than *Uqcrcq*^{ff} mice (Figures 7K, S7P-S7R). Their cholesterol and ALT levels in
386 plasma as well as their hepatic lipid content was also reduced (Figures S7S-S7U). Notably, HFD-
387 fed *CD11cΔUqcrcq* mice displayed elevated brown adipose tissue (BAT) thermogenesis (Figure
388 7L). Together with the higher expression of lipid catabolism-related genes in eWAT and enhanced
389 released CO₂ volume of HFD-fed *LysMΔTfam* vs *Tfam*^{ff} mice (Figures 7G, 7H and S7C), this
390 observation suggests that a decrease of pro-inflammatory eWAT-MFs due to OXPHOS
391 interference in obesity causes improved eWAT functionality, removal of excess lipids by oxidation
392 as well as heat production via the BAT (Bae et al., 2018; Matesanz et al., 2018). In summary,
393 OXPHOS dysfunction specifically reduces pro-inflammatory TMFs in obese eWAT, which handle

394 high amounts of lipids, by inducing cellular stress and impairing their proliferation. This results in
395 mitigation of inflammation, metabolic dysfunction and hepatosteatosis.

396 Discussion

397 Overall, we uncovered a metabolic diversity in both human and mouse TMFs in vivo during
398 homeostasis, and OXPHOS as the main distinguishing feature among TMFs located in different
399 organs. The high contribution of OXPHOS to the bioenergetics of AMs and LPMs compared with
400 BMDMs is established (Davies et al., 2017; Izquierdo et al., 2018; Svedberg et al., 2019; Wculek
401 et al., 2022; Woods et al., 2020) and AMs do not enhance glycolysis upon LPS stimulation (Woods
402 et al., 2020), whereas opposing effects of *Tfam* deletion in AMs were reported (Gao et al., 2022;
403 Soberanes et al., 2019). Our study unambiguously reveals OXPHOS as an important determinant
404 for identity and maintenance of specific TMF populations in the steady state. We detected the
405 induction of cellular and ER stress in affected *Tfam*-deficient TMFs, demonstrated by activation
406 of *Atf4*, that likely accounts for their increased apoptosis and reduced proliferation. Interestingly,
407 ATP levels in OXPHOS-dependent *Tfam*-deficient TMFs are unaltered, but, at least in AMs,
408 become dependent on glycolysis to fulfil their bioenergetic demands. However, an enhanced
409 glycolytic metabolism per se in AMs did not phenocopy the cellular stress and apoptosis caused
410 by *Tfam* deletion (Izquierdo et al., 2018). Regarding OXPHOS, the adaption of the usage of ETC
411 complex I and II upon bacterial sensing regulates the functions of BMDMs (Garaude et al., 2016)
412 and the complex I protein *Ndufs4* was shown to control inflammatory macrophage and osteoclast
413 polarisation (Jin et al., 2014). Interestingly, in contrast to complex II, III, and IV, complex I is the
414 only ETC complex that is dispensable for the maintenance of *Tfam* deletion-sensitive TMFs. This
415 points to an essential role of the correct functioning of the TCA cycle and a complex II-driven
416 ETC for the activity and maintenance of AMs and other OXPHOS-dependent TMFs. The
417 normalization of *Atf4* levels and proliferation upon culture of *Tfam*-deficient AMs ex vivo,
418 suggested a microenvironment-triggered effect that determines the vulnerability of certain TMFs
419 to OXPHOS impairment during homeostasis.

420 Efferocytosis of dying cells by macrophages provides FAs and fuels mitochondrial respiration
421 during tissue injury. Yet, this induces anti-inflammatory functions, not cellular stress and
422 apoptosis, in cultured BMDMs or cardiac macrophages (Zhang et al., 2019). Homeostatic *Tfam*-
423 deficient AMs did not accumulate free FAs, but larger lipid species reminiscent of extracellular
424 surfactant and free cholesterol. Elevated lipid levels, especially of cholesterol, is a potent cause of
425 cellular stress and *Atf4* activation in macrophages (Feng et al., 2003; Tabas, 2002; Yao et al.,
426 2014). Notably, we show that a reduction of systemic lipid and cholesterol levels in *CD11cΔTfam*
427 mice improves AM and RPM numbers. Our analysis reveals a significant correlation of OXPHOS
428 and cholesterol handling-related gene expression across human and mouse TMF populations.
429 Hence, we uncovered the need for a functional ETC and OXPHOS in TMFs for handling of
430 extracellular lipids/cholesterol to maintain homeostasis. In line with this, the TMFs that are most
431 affected by *Tfam* deficiency; AMs, LPMs, RPMs, and KCs; display a high activity and/or
432 expression of genes required for lipid metabolism and handling (Remmerie and Scott, 2018;
433 Wculek et al., 2022). Moreover, the loss of peroxisome proliferator-activated receptor (PPAR) γ
434 and/or LXR α and β , the master regulators of lipid catabolism and intracellular cholesterol
435 handling, causes a comparable phenotype as *Tfam* deletion in AMs, RPMs and/or KCs (Schneider
436 et al., 2014; Schuster et al., 2002).

437 Finally, we also revealed the relevance of OXPHOS for the maintenance of extracellular lipid-
438 handling TMFs in the pathologic setting of overnutrition-induced obesity. In contrast to lean WAT,

439 adipocytes die in obese eWAT and release lipids that change the microenvironment. eWAT-MFs
440 become bioenergetically activated (Boutens et al., 2018; Serbulea et al., 2018) and form CLS
441 around adipocytes to clear the released lipids. Those obese eWAT-MFs in CLS express CD11c
442 and CD9, accumulate lipids, and become pro-inflammatory (Hill et al., 2018; Li et al., 2010;
443 Wculek et al., 2022; Yang et al., 2020). Interference with increases in intracellular ROS can impair
444 proinflammatory macrophage activation (Mills et al., 2016). While we observed elevated ROS
445 levels at baseline in *Tfam*-deficient TMFs, we cannot entirely exclude a potential contribution of
446 alterations of ROS levels to the reduction of proinflammatory *LysMΔTfam* eWAT-MFs. Fgr kinase
447 deletion in bone marrow cells imbalances complex I/II usage by the ETC and alters polarization
448 of eWAT-MFs, decreasing pro-inflammatory and increasing anti-inflammatory macrophage
449 presence (Acín-Pérez et al., 2020). Notably, *Tfam* deficiency only diminished the numbers of pro-
450 inflammatory, lipid-handling eWAT-MFs in obese WAT by specifically inducing cellular stress
451 and decreasing their local proliferation, but not that of anti-inflammatory eWAT-MFs or lean
452 WAT-MFs. While we focused on analysis of embryo-derived TMFs in the steady state as they
453 represent stable populations, this finding suggests a vital role of mitochondrial respiration, not
454 glycolysis, for the maintenance of pro-inflammatory monocyte-derived macrophages in obesity.
455 In line with this, cultured M1 BMDMs accumulate more cholesterol than M2 BMDMs and the
456 lipid profile of obese CD9⁺ WAT-MFs is distinct from that of other recruited WAT-MFs (Morgan
457 et al., 2021). Pro-inflammatory CD9⁺ WAT-MFs can induce an inflammatory phenotype in WAT
458 (Hill et al., 2018) and are important drivers of obesity-associated pathologies (Dahik et al., 2020;
459 Korf et al., 2019). Thus, we find that HFD-fed *LysMΔTfam* mice show reduced signs of
460 inflammation and are markedly protected from insulin resistance and hepatosteatosis.

461 In conclusion, we propose a selective function of OXPHOS for the maintenance of homeostatic
462 TMFs with a high demand of lipid handling activity. This metabolic dependency on mitochondrial
463 respiration also affects pro-inflammatory TMF populations that promote pathologies. Hence,
464 pharmacological interference with OXPHOS in such TMFs, for example via specific targeting of
465 mitochondrial inhibitors, holds promise for therapeutic exploration to ameliorate metabolic
466 syndrome.

467 **Acknowledgments:**

468 We are grateful to N-G. Larsson, F. Sánchez-Madrid, G. Sabio, R.D. Palmiter, E. Gottlieb, C.T.
469 Moraes and M.A. del Pozo for sharing essential reagents. We thank S. Iborra, his team, M.
470 Sánchez-Álvarez, I. Nikolic and members of the DS laboratory for discussions and critical reading
471 of the manuscript. We thank the staff at the CNIC technical units; foremost the animal, cellomics,
472 histology, metabolomics, genomics, microscopy and bioinformatics facilities; and the SIdI of the
473 Universidad Autónoma de Madrid for technical support.

474 **Funding:**

475 This project was supported by the "La Caixa" Foundation (ID 100010434) Postdoctoral Junior
476 Leader Fellowship code LCF/BQ/PR20/11770008 (SKW); "La Caixa" Foundation (ID
477 100010434) INPhINIT Fellowship code LCF/BQ/IN17/11620074 (IHM); Spanish Ministry of
478 Education FPU fellowship code FPU20/01418 (MG); Ministerio de Ciencia e Innovación (MCIN)
479 PID2019-104233RB-100/AEI/10.13039/501100011033 (SL); NIH grants P01AG049665-08,
480 RO1A148190 and P01HL154998 (NSC).

481 The work JAE laboratory is supported by the CNIC and a grant by Ministerio de Ciencia,
482 Innovación e Universidades (MCNU), Agencia Estatal de Investigación (AEI) and Fondo Europeo
483 de Desarrollo Regional (FEDER) (RTI2018-099357-B-I00), the Biomedical Research Networking
484 Center on Frailty and Healthy Ageing (CIBERFES-ISCiii- CB16/10/00289) and the HFSP agency
485 (RGP0016/2018).

486 Work in the DS laboratory is funded by the CNIC; by the European Union's Horizon 2020 research
487 and innovation programme under grant agreement ERC-2016-Consolidator Grant 725091; by
488 MCIN PID2019-108157RB/AEI/10.13039/501100011033; by Comunidad de Madrid
489 (B2017/BMD-3733 Immunothercan-CM); and by "la Caixa" Foundation (LCF/PR/HR20/00075).
490 The CNIC is supported by the Instituto de Salud Carlos III (ISCIII), the MICINN and the Pro
491 CNIC Foundation, and is a Severo Ochoa Center of Excellence (CEX2020-001041-S funded by
492 MCIN/AEI /10.13039/501100011033).

493 **Author contributions:**

494 Conceptualization: SKW, IHM, DS

495 Methodology, investigation, analysis, visualization, and validation: SKW, IHM, AM, DM, MG,
496 SL, VM, AC

497 Essential reagents and support: CB, JAE, NSC

498 Writing of original draft: SKW, DS

499 Funding acquisition, supervision, and project administration: SKW, DS

500 Editing of draft: all authors

501 **Declaration of interests:** Authors declare that they have no competing interests.

502

Figure legends

503

Figure 1. Mitochondrial OXPHOS metabolism is a main distinctive signature of different TMF populations.

504

(A) Schematic representing the workflow used in the pseudo-bulk-based analysis of human TMF clusters.

506

(B) PCA of scRNAseq data from the Human Cell Landscape of previously identified TMF clusters of indicated human organs. Dots represent individual pseudo-bulked samples.

507

(C and D) Pre-ranked gene set-enrichment analysis of the genes defining PC1 in the analysis shown in (B) using Gene Ontology (GO) biological processes (C) and gene set-enrichment plot of OXPHOS-related genes (KEGG reference pathway hsa00190, D). NES, normalized enrichment score; Adj., adjusted with Benjamini–Hochberg correction.

509

(E) PCA of RNAseq data from the Immunological Genome Project of indicated mouse TMF populations. Dots represent individual samples.

510

(F and G) Pre-ranked gene set-enrichment analysis of the genes defining PC1 in the analysis shown in (E) using GO biological processes (F) and gene set-enrichment plot of OXPHOS-related genes (KEGG reference pathway mmu00190, G).

511

(H) Heatmap of log-Fold change (FC) of detected mt-genes (calculated comparing each individual tissue with the mean of all tissues) and their average in the mouse TMF population RNAseq data analysis shown in (E). * $p < 0.05$, by Moderated t-test. See also Figure S1 and S2.

512

513

514

515

516

517

518

519

520

Figure 2. OXPHOS impairment has different effects on distinct TMF populations in homeostasis.

521

(A to D) *Tfam* mRNA levels (A) mt-DNA levels (B) flow cytometric quantification of numbers (C) and frequency (D) of the indicated TMF populations in lean adult *CD11cΔTfam* or *LysMΔTfam* relative to *Tfam^{fl/fl}* mice (n=3-9). Flow cytometric identification of TMFs is detailed in methods and Langerin⁺ cell numbers (LCs, n=8-11) in (C) were quantified by fluorescence microscopy of epidermal sheets.

522

(E) Pearson's correlation of the average percentage of number reduction in organs of *CD11cΔTfam* or *LysMΔTfam* relative to *Tfam^{fl/fl}* mice (C) and average levels of detected mt-gene expression (Figure 1H) of the indicated mouse TMF populations.

523

(F) Relative median intensity of autofluorescence determined by flow cytometry of the indicated TMF populations in lean adult *CD11cΔTfam* or *LysMΔTfam* relative to *Tfam^{fl/fl}* mice (n=3-9).

524

Data in (A to D and F) were normalized to the respective *Tfam^{fl/fl}* controls for each TMF population to facilitate comparisons. For orientation, OXPHOS-interference insensitive and sensitive TMFs are separated by a gap in the graphs. Data are merged from at least 2 independent experiments and presented as mean ± SEM. Dots represent individual data points. Statistical analysis by unpaired Student's t-test (A-D and F) or Pearson's correlation test (E). * $p \leq 0.05$, ** $p \leq 0.01$, *** $p \leq 0.001$; ns, not significant.

525

526

527

528

529

530

531

532

533

534

535

536

537

538

Figure 3. Impaired proliferation and increased apoptosis in *Tfam*-deficient AMs is not caused by a bioenergetic crisis, but is linked to a TCA cycle deregulation.

539

2 day-old, 11 day-old, 3 week (wk)-old or adult (6-8 week-old) *Tfam^{fl/fl}* and *CD11cΔTfam* mice or their AMs in the lung were analyzed.

540

(A to C) Flow cytometric quantification of numbers (A, n=4-9), relative median fluorescence intensity (MFI) of autofluorescence (AF), Siglec F or CD11b (B, n=4-8) as well as representative plots of F4/80⁺ CD11c⁺ cells in the lungs of adult mice (C, gated on CD45⁺).

541

(D) BAL turbidity evaluated visually (photograph, top) and by optical density (OD, bottom) (n=7-8).

542

543

544

545

546

547

548 (E and F) Flow cytometric quantification and representative plots of frequency of Ki67⁺ (E) or
549 activated caspase 3⁺ cells (F) in CD11c⁺ cells in BAL of 3 week-old mice (n=5-7).
550 (G) Oxygen consumption rate (OCR) of CD11c⁺ cells from BAL of adult mice (n=3 merged from
551 5-10 mice).
552 (H) Quantification of mitochondrial membrane potential ($\Delta\Psi_m$) and representative images of
553 fluorescence microscopy of tetramethylrhodamine, methyl ester (TMRM, red), CD11c (green) and
554 Hoechst 33342 (blue) staining of CD11c⁺ cells from BAL of adult mice (scale bar: 20 μ m, n=3
555 [mean of 54-231 cells/mouse]).
556 (I) ATP levels in F4/80⁺ CD11c⁺ cells from the lung of 3 week-old mice (n=6-8).
557 (J) Lactate levels and picture of the supernatant of CD11c⁺ cells from BALs of adult mice cultured
558 for 3 days (n=4, merged from 5-10 mice).
559 (K) Extracellular acidification rate (ECAR) of CD11c⁺ cells from BALs of adult mice (n=3 merged
560 from 5-10 mice).
561 (L) Relative abundance of the indicated TCA cycle intermediates in F4/80⁺ CD11c⁺ cells from
562 BAL of adult mice (n=3 merged from 13-30 mice).
563 (M) Heat map of expression levels of deregulated (Adj. p-value <0.05) TCA cycle-related (KEGG
564 mmu00020) genes detected in the RNAseq of FACS-sorted CD45⁺ F4/80⁺ CD11c⁺ lung cells from
565 3 week-old *Tfam*^{ff} and *CD11c* Δ *Tfam* mice.
566 (N and O) Flow cytometric quantification of numbers (N) and relative MFI of Siglec F (O, left) or
567 CD11b (O, right) of CD45⁺ F4/80⁺ CD11c⁺ cells in the lung of adult *CD11c* Δ *Ndufs4* mice,
568 *CD11c* Δ *Sdhb* mice, *CD11c* Δ *Uqcrq* or *CD11c* Δ *Cox10* mice compared with their control littermates
569 (n=4-8).
570 Data are merged from at least 2 independent experiments and presented as mean \pm SEM. Dots
571 represent individual data points. Statistical analysis by unpaired (A-H, J and L-O) or paired (K)
572 Student's t-test or one-way ANOVA with Tukey correction (I). *p \leq 0.05, **p \leq 0.01, ***p \leq 0.001.
573 See also Figure S3 and S4.

574 **Figure 4. Extrinsic tissue microenvironmental factors induce cellular stress and a cell cycle**
575 **block in OXPHOS-impaired AMs.**

576 3 week (wks)-old or adult *Tfam*^{ff} and *CD11c* Δ *Tfam* mice or their AMs in the lung were analyzed.
577 (A) Heat map of expression levels of deregulated genes included in the “intrinsic apoptotic
578 signaling pathway in response to endoplasmic reticulum (ER) stress” (GO process GO:0070059)
579 pathway detected to be significantly deregulated in the RNAseq of FACS-sorted CD45⁺ F4/80⁺
580 CD11c⁺ lung cells from 3 week-old mice.
581 (B) *Atf4* expression levels detected in RNAseq data (n=4) of CD45⁺ F4/80⁺ CD11c⁺ lung cells
582 from 3 week-old mice.
583 (C) Quantification and representative gel electrophoresis of *Xbp1* splice isoforms detected by PstI-
584 restriction of a PCR product amplified from cDNA of FACS-sorted CD45⁺ F4/80⁺ CD11c⁺ lung
585 cells from 3 week-old mice (n=5-7).
586 (D to F) CD11c⁺ cells were magnetically purified from BAL of 3 week-old mice and either directly
587 analyzed (Day 0) or cultured for 48h before analysis of *Atf4* (D) or *Cdk1* and *Ccnb2* mRNA levels
588 (E) or flow cytometric analysis of Ki67⁺ cells (F, representative plot and quantification) (n=4
589 merged from 2-4 mice).
590 Data are merged from at least 2 independent experiments and presented as mean \pm SEM. Dots
591 represent individual data points. Statistical analysis by unpaired Student's t-test. *p \leq 0.05,
592 **p \leq 0.01, ***p \leq 0.001. See also Figure S5.

593 **Figure 5. Environmental lipids and cholesterol accumulate in *Tfam*-deficient AMs and cause**

594 **the decline of their population.**
595 3 week (wks)-old or adult *Tfam^{ff}* and *CD11cΔTfam* mice or their AMs in the lung were analyzed.
596 (A) Flow cytometric quantification of relative MFI (n=7), representative plots and images of
597 fluorescence microscopy (scale bar: 20μm) of Nile-Red staining of CD11c⁺ cells from BAL of
598 adult mice.
599 (B) Representative images of transmission electron microscopy of and quantification of spiral-like
600 structures in FACS-sorted F4/80⁺ CD11c⁺ cells from BAL of adult mice (n=16-24 cells from 4-9
601 mice).
602 (C) Radiolabeled palmitate-derived CO₂ after incubation of CD11c⁺ cells from BAL of adult mice
603 with ¹⁴C-palmitate (n=4 merged from 5-10 mice).
604 (D and E) Heat map of expression levels of selected FA degradation- (D) and cholesterol handling-
605 related genes (E) detected in RNAseq of CD45⁺ F4/80⁺ CD11c⁺ lung cells from 3 week-old mice.
606 (F) Relative abundance of cholesterol in F4/80⁺ CD11c⁺ cells from BAL of adult mice detected by
607 GC/MS analysis (n=3 merged from 13-30 mice).
608 (G) Cholesterol uptake (left) and relative efflux (right) after incubation of CD11c⁺ cells from BALs
609 of adult mice with fluorescently-labelled cholesterol (n=3 merged from 5-10 mice).
610 (H and I) Quantification of total cholesterol levels (H) and flow cytometric quantification of
611 numbers of F4/80⁺ CD11c⁺ cells (I) in BAL of mice treated with Simvastatin or control DMSO
612 for 8 weeks (n=5-13).
613 Data are merged from at least 2 independent experiments and presented as mean ± SEM. Dots
614 represent individual data points. Statistical analysis by unpaired (A, F and H) or paired (C and G)
615 Student's t-test. *p≤0.05, **p≤0.01, ***p≤0.001. See also Figure S6.

616 **Figure 6. High cholesterol handling activity determines the vulnerability of tissue**
617 **macrophages to OXPHOS impairment.**

618 (A) Langerin⁺ cell numbers (LCs) quantified by fluorescence microscopy of epidermal sheets (left,
619 n=4-9) and flow cytometric quantification of numbers of F4/80⁺ CD11b^{low} MHCII^{low} cells (RPMs)
620 in the spleen (right, n=5-7) of adult *CD11c^{Cre} Ndufs4^{ff/-}* relative to *Ndufs4^{ff/-}* mice, *CD11c^{Cre} Sdhb^{ff/ff}*
621 relative to *Sdhb^{ff/ff}* mice, *CD11c^{Cre} Uqcrcq^{ff/ff}* relative to *Uqcrcq^{ff/ff}* mice or *CD11c^{Cre} Cox10^{ff/ff}* relative
622 to *Cox10^{ff/ff}* mice.
623 (B) ATP levels in FACS-sorted CD11b⁺ MHCII^{low} F4/80^{high} cells from the peritoneal lavage
624 (LPMs) of adult *Tfam^{ff/ff}* and *LysMΔTfam* mice (left, n=4-5) and in FACS-sorted F4/80⁺ CD11b^{low}
625 MHCII^{low} cells from the spleen (RPMs) of adult *Tfam^{ff/ff}* and *CD11cΔTfam* mice (right, n=4-6).
626 (C) Flow cytometric quantification of relative MFI of Nile-Red staining of F4/80^{high} cells from the
627 peritoneal lavage (LPMs) of adult *Tfam^{ff/ff}* and *LysMΔTfam* mice (left, n=6-8) and of magnetically
628 purified F4/80⁺ cells from the spleen (RPMs) of adult *Tfam^{ff/ff}* and *CD11cΔTfam* mice (right, n=9-
629 10).
630 (D) Analysis of *Atf4* mRNA levels in FACS-sorted CD11b⁺ MHCII^{low} F4/80^{high} cells from the
631 peritoneal lavage (LPMs) of adult *Tfam^{ff/ff}* and *LysMΔTfam* mice (left, n=7-8) and in FACS-sorted
632 F4/80⁺ CD11b^{low} MHCII^{low} cells from the spleen (RPMs) of adult *Tfam^{ff/ff}* and *CD11cΔTfam* mice
633 (right, n=8-9).
634 (E) Flow cytometric quantification of frequencies (left) and numbers (right) of F4/80⁺ CD11b^{low}
635 MHCII^{low} cells in the spleen (RPMs) of *Tfam^{ff/ff}* and *CD11cΔTfam* mice treated with Simvastatin
636 or control DMSO for 8 weeks (n=10-13).
637 (F) Pearson's correlation of expression of OXPHOS-related genes (KEGG pathway mmu00190)
638 and genes regulating cholesterol transport (GO process GO:0032376) or fatty acid catabolism (GO
639 process GO:0009062) in mouse TMF populations using RNAseq data (see Figure 1E).
640 (G) Pearson's correlation of expression of OXPHOS-related genes (KEGG pathway hsa00190)

641 and genes regulating cholesterol transport (GO process GO:0032367), cellular lipid catabolism
642 (GO process GO:0044242) or fatty acid catabolism (GO process GO:0009062) in TMF clusters
643 identified in the scRNAseq data of indicated human organs (see Figure 1A).
644 (H) Diagram of proposed mechanism. FAO, fatty acid oxidation.
645 Data are merged from at least 2 independent experiments and presented as mean \pm SEM. Dots
646 represent individual data points. Statistical analysis by unpaired (A-E) Student's t-test or Pearson's
647 correlation test (F and G). * $p \leq 0.05$, ** $p \leq 0.01$, *** $p \leq 0.001$.

Figure 7. OXPHOS dysfunction reduces pro-inflammatory eWAT-MF presence during obesity and prevents metabolic syndrome and hepatosteatosis.

650 *Tfam^{ff}* and *LysM Δ Tfam* or *Uqcrcq^{ff}* and *CD11c Δ Uqcrcq* mice were fed an HFD for 9 weeks and
651 analyzed.

652 (A) Quantification and representative images of magnetic resonance imaging to determine body
653 mass (n=17).

654 (B) *Atf4* mRNA levels after FACS-sorting (left, n=5-6) or flow cytometric analysis of Ki67⁺ (right,
655 n=11) in CD64⁺ F4/80⁺ and CD206⁺ or CD9⁺ cells from eWAT.

656 (C) Flow cytometric quantification of numbers and representative plots of gated CD45⁺ CD64⁺
657 F4/80⁺ cells (that also express indicated markers) in eWAT (n=13-15).

658 (D) Quantification and representative image of F4/80 (brown) and hematoxylin (blue)-stained
659 eWAT sections (scale bar: 500 μ m, n=12-13).

660 (E) *Tnfa* and *Ccl2* mRNA levels in eWAT (n=10-16).

661 (F) White blood cell (WBC) counts in blood (n=13-15).

662 (G and H) mRNA levels of selected lipid metabolism (G) or mitochondrial respiration-related
663 genes (H) in eWAT (n=6-13).

664 (I) Glucose levels measured over time in blood after intraperitoneal injection (time = 0) of insulin
665 (n=13-16).

666 (J) Quantification and representative image of Oil-Red O (red) and hematoxylin (blue)-stained
667 liver sections (scale bar: 100 μ m, n=8-9).

668 (K) Flow cytometric quantification of numbers of CD45⁺ CD64⁺ F4/80⁺ cells (that also express
669 indicated markers) in eWAT (n=18).

670 (L) Quantification of maximal and average temperature and representative infrared thermal images
671 of the BAT area of obese mice (n=6-8).

672 Data are merged from at least 2 independent experiments and presented as mean \pm SEM. Dots
673 represent individual data points. Statistical analysis by unpaired Student's t-test (A-H and J-L) or
674 two-way ANOVA with Geisser-Greenhouse correction (I). * $p \leq 0.05$, ** $p \leq 0.01$, *** $p \leq 0.001$. See
675 also Figure S7.

676 **STAR Methods**

677 **RESOURCE AVAILABILITY**

678 ***Lead contact***

679 Further information and requests for resources and reagents should be directed to and will be
680 fulfilled by the lead contact, David Sancho (dsancho@cnic.es).

681 ***Materials availability***

682 The gene expression and metabolomics data generated and the code used in this study are available
683 at Gene Expression Omnibus (GEO), Metabolomics workbench or Zenodo, respectively (details
684 see key resources table). There are restrictions to the availability of the following mouse strains
685 because they were obtained under a material transfer agreement: with N-G. Larsson (Max Planck
686 Institute for Biology of Ageing, *Tfam^{ff}*), R.D. Palmiter (University of Washington, *Ndufs4^{ff}*), E.
687 Gottlieb (Beatson Institute for Cancer Research, *Sdhb^{ff}*), and C. T. Moraes (University of Miami,
688 *Cox10^{ff}*). This study did not generate other new unique reagents.

689 ***Data and code availability***

690 This paper analyzes existing, publicly available data. These accession numbers for the datasets are
691 listed in the key resources table.

692 Bulk RNA-seq data have been deposited at GEO and metabolomics data at Metabolomics
693 workbench and are publicly available as of the date of publication. Accession numbers are listed
694 in the key resources table. All other data are available in the main text, STAR methods and
695 supplementary materials or will be shared by the lead contact upon request.

696 Code used for transcriptomics analysis has been deposited at Zenodo and is publicly available as
697 of the date of publication. DOIs are listed in the key resources table.

698 Any additional information required to reanalyze the data reported in this paper is available from
699 the lead contact upon request.

700 **EXPERIMENTAL MODEL AND SUBJECT DETAILS**

701 ***Mice***

702 Mouse colonies were bred at the CNIC under specific pathogen-free conditions and on C57BL/6
703 background. *Tfam^{ff}* (Larsson et al., 1998), *Ndufs4^{ff}* (Kruse et al., 2008) and *Sdhb^{ff}* (Cardaci et al.,
704 2015) mice were kindly provided by Nils-Göran Larsson (Max Planck Institute for Biology of
705 Ageing, Cologne, Germany), Richard D. Palmiter (University of Washington, Seattle, USA), and
706 Eyal Gottlieb (Beatson Institute, Glasgow, UK), respectively. *Ndufs4^{ff}* mice were created by
707 crossing floxed males with *Zp3^{Cre}* females (Lewandoski et al., 1997). All floxed mouse lines, as
708 well as *Uqcrcq^{ff}* (Weinberg et al., 2019) and *Cox10^{ff}* (Diaz et al., 2005) mice, were crossed with
709 *CD11c^{Cre}* (Caton et al., 2007) or *LysM^{Cre}* mice (Clausen et al., 1999). Mice were group-housed,
710 have not been used in previous procedures and were fed standard chow except for experiments
711 using high fat diet (as indicated and see below). Littermates of the same sex were randomly
712 assigned to experimental groups. Male and female mice were used for all experiments, except
713 experiments using high fat diet (as indicated and see below). Mice with the following ages were
714 used for all experiments (as indicated): 2 days, 11 days, 3 weeks or 6–10-weeks (adult). The local
715 ethics committee approved all animal studies. All animal procedures conformed to EU Directive
716 86/609/EEC and Recommendation 2007/526/EC regarding the protection of animals used for
717 experimental and other scientific purposes, enforced in Spanish law under Real Decreto
718 1201/2005.

719 ***Primary cell culture***
720 Primary cells were obtained from the above-mentioned male and female mice and the experimental
721 methods are described in the Methods Details section. Cells were cultured at 37°C with 5% CO₂
722 in R10 medium [RPMI Medium 1640 (Gibco) with 10% FBS, 2 mM L-Glutamine, 100 U/mL
723 Penicillin and Streptomycin (100 µg both Lonza) and 1 mM Sodium Pyruvate (HyClone™)] on
724 Fibronectin-coated cell culture plates or glass slides for up to 72 hours, as indicated for individual
725 experiments. Culture media was supplemented with 0.1 ng/ml recombinant murine GM-CSF for
726 experiments using cells from 3 week-old mice and inhibitors or small molecules were added as
727 outlined in the Methods Details section.

728 **METHOD DETAILS**

729 ***Animal procedures***

730 Simvastatin treatment: 3 week-old mice received daily intraperitoneal injections of 10 mg/kg
731 Simvastatin in 10% DMSO in PBS for 8 weeks before all analyses, except for AM proliferation
732 and apoptosis which were analysed after 3 weeks.

733 High fat diet experiments: 7-8 week-old males were changed to Rodent Diet with 60% kcal Fat
734 (D12492, Research Diets Inc) for 9 weeks before perfusion and analysis. At week 7-9 after diet
735 change, the following tests were performed:

736 For glucose or insulin tolerance tests, mice were fasted for 16 hours before intraperitoneal injection
737 of 2 g/kg glucose (Sigma) or 0.75 U/kg insulin (Humulina regular), respectively. Blood glucose
738 levels were measured by bleeding from the tail vein using a handheld glucose meter (Contour
739 Next, Bayer) at indicated times.

740 Food and water intake, consumed O₂ volume, expired CO₂ volume, respiratory exchange ratio and
741 energy expenditure of mice were determined by an indirect calorimetry system (TSE LabMaster,
742 TSE Systems, Germany) for 48-72 hours after a 2-day acclimatization and analyzed using
743 METABOLISM Software (Panlab).

744 Biomedical Imaging was conducted at the Advanced Imaging Unit of the CNIC and this project
745 used the ReDIB ICTS infrastructure TRIMA@CNIC, Ministerio de Ciencia e Innovación. Body,
746 fat, and lean mass were quantified by magnetic resonance imaging (MRI) using a small animal
747 magnetic resonance scanner 7 Tesla (Varian) and analyzed by ImageJ/Fiji software.

748 For determination of maximal and average BAT-adjacent interscapular temperature, the skin
749 around the BAT area of mice was shaved 24 hours before taking 5 thermographic images per
750 animal using a FLIR T430sc Infrared Camera (FLIR Systems, Inc., Wilsonville, OR), which were
751 analyzed using FLIR R&D software.

752 ***Tissue dissociation for cell isolation***

753 Lungs were minced and incubated for 20 min in HBSS (Gibco); ear skin layers were separated,
754 minced and digested for 30 min in HBSS; kidneys were minced and incubated for 30 min in FACS
755 buffer [3% heat-inactivated Fetal Bovine Serum (FBS), 0.5mM EDTA (both Sigma) in PBS
756 (Gibco)] and spleens were digested for 10 min in R10 medium. Digestions were done with 0.25
757 mg/ml Liberase TL and 50 µg/ml DNaseI with shaking at 37°C. Minced adipose tissue (eWAT
758 and iWAT) was incubated for 20 min in 50:50 PBS/HBSS with 0.5% BSA (Sigma) and 2 mg/ml
759 collagenase type 2 and minced livers were digested for 20 min in HBSS with 0.5% BSA, 1 mg/ml
760 Collagenase A and 50 µg/ml DNaseI with shaking at 37°C. To obtain single cell suspensions, ear
761 skin was passed 5 times through a 18g syringe, adipose tissue was triturated 5 times with a 10 ml
762 pipette and all tissues were squeezed through a 70 or 100 µm cell strainer (Corning). Peritoneal

763 cells were collected by lavage of the peritoneum with 8-10 ml PBS. Bronchoalveolar lavage (BAL)
764 was performed by inserting a venal catheter (BD) into the trachea and 3-10 washes with 0.3-1 ml
765 FACS buffer to harvest BAL cells. Blood was harvested by bleeding from the submaxillary vein
766 or cardiac puncture. All cell suspensions were subjected for 1-5 min (blood 3 times) to Red Blood
767 Cell Lysing Buffer, washed with FACS buffer and re-filtered through a 40 μ m cell strainer and
768 either directly analyzed or further processed.

769 ***Flow cytometry and cell sorting***

770 Single cell suspensions were incubated for 20 min at 4°C in PBS with 2% heat inactivated-FBS
771 and 0.5 mM EDTA (Sigma) with FcR block anti-mouse CD16/CD32 antibody and a mix of
772 fluorochrome-conjugated antibodies as indicated in the key resources table. DAPI was used to
773 exclude dead cells. Autofluorescence was determined using the UV or blue laser.

774 After antibody incubation, cells were stained with Nile-Red (1 μ g/ml in PBS) for 10 min at room
775 temperature (RT) or with Dihydroethidium (DHE, 20 μ M in R10 without Phenol Red or FBS) for
776 1 hour at 37°C, for ROS determination. For intracellular staining related to apoptosis, the Active
777 Caspase-3 Apoptosis Kit was used according to manufacturers' instructions in combination with
778 anti-active Caspase-3 (clone C92-605) and/or Ki67 (clone SolA15) antibodies. The LSRFortessa
779 or FACSymphony cell analyzers running FACSDiva software and FlowJo Version 10 software
780 were used to record and analyze data.

781 For FACS cell sorting: lung or spleen single cell suspensions were incubated with mouse CD11c
782 MicroBeads UltraPure or Anti-F4/80 MicroBeads UltraPure, respectively, loaded onto LS
783 columns and the positive fraction collected according to manufacturers' instructions before
784 fluorescent staining. Immune cells from kidney cell suspensions were enriched using a density
785 gradient centrifugation (Bicoll cell separation solution, 700 xg centrifugation for 30 min at RT).
786 Cells were flow-sorted using the FACSARIA II cell sorter running FACSDiva software.

787 TMF populations were identified as follows: F4/80⁺ CD64⁺ CD206⁺ or CD9⁺ cells in iWAT and
788 eWAT (iWAT-MFs, eWAT-MFs); CD45⁺ F4/80⁺ CD64⁺ cells in kidney (KMs); F4/80⁺ CD11b^{low}
789 MHCII^{low} cells in spleen (RPMs); CD45⁺ Siglec F⁻ Ly6G⁻ Ly6C⁻ F4/80⁺ cells in liver (KCs); CD64⁻
790 MHCII⁺ CD11b⁺ CD24⁺ cells in CD45⁺ cells in skin (LCs); CD11b⁺ MHCII^{low} F4/80^{high} cells in
791 peritoneal lavage (LPMs) and CD45⁺ F4/80⁺ CD11c⁺ cells in lung (AMs).

792 For magnetic MACS cell sorting of BAL: AMs were purified using mouse CD11c MicroBeads
793 UltraPure and MS columns according to manufacturers' instructions.

794 ***Analysis of single cell RNA sequencing***

795 All RNA-seq-related analyses were performed in R (version 4.2.1). Single-cell RNA-seq raw
796 counts data from the Human Cell Landscape project were downloaded from
797 https://figshare.com/articles/HCL_DGE_Data/7235471. After selecting datasets based on the
798 health status of the donors and absence of inflammatory cell infiltrates to ensure homeostatic
799 samples (Figure S1A), cells annotated as TMFs were independently analyzed using Bioconductor
800 packages (Huber et al., 2015) and Seurat (Butler et al., 2018). After ruling out cells with poor
801 quality metrics (counts \geq 400 and \leq 3000, detected genes \geq 200 and \leq 1250, and % of mitochondrial
802 genes \leq 15), further analysis of resulting TMFs were performed at the pseudo-bulk level by
803 aggregating cells according to the tissue of origin. Single-cell profiles were summarized by
804 averaging counts per million (CPM) in order to force all cells to contribute with the same extent.
805 The number of pseudo-replicates for every tissue was determined by keeping a similar number of
806 detected genes per pseudo-bulk sample. Finally, pseudo-bulk samples were transformed with
807 logarithm to the base 2 for further analysis.

808 Log₂(CPM) pseudo-bulk samples were scaled and used as input for principal component analysis
809 (PCA). Genes were ranked according to the loading vectors of each PC. Resulting ranks were used
810 as input for the FGSEA algorithm along with the Kyoto Encyclopedia of Genes and Genomes
811 (KEGG) (www.genome.jp/kegg) and Gene Ontology (GO) (www.geneontology.org/) databases
812 in order to identify the main sources of variability detected by PCA. Only gene sets with a number
813 of genes ≥ 15 and ≤ 500 were considered for PCA-based enrichment analysis.

814 Gene set analysis was performed using log-fold changes as per gene statistics as previously
815 described (Luo et al., 2009). In summary, log-fold changes for every gene were calculated
816 comparing each TMF population to the background (rest of TMFs). Then, gene set enrichment
817 scores in each TMF population were calculated as T-scores (two-sample T-test) comparing the
818 corresponding mean log-fold changes of each gene set with all genes (background). Finally,
819 Pearson's correlations between T-scores of different gene sets were calculated using R.

820 ***Bulk RNA sequencing and analysis***

821 Analysis of bulk RNA-seq data was performed in R (version 4.1.2) using the Bioconductor
822 package Limma for normalization (using TMM method) and differential expression testing
823 (moderated t-test and Benjamini–Hochberg correction with adjusted p-value ≤ 0.05 as criterion for
824 differentially expressed genes), taking only those genes into account that were expressed with at
825 least 1 CPM. For the differential analysis of TMFs, raw counts generated by the Immunological
826 Genome Project were downloaded from Gene Expression Omnibus (GEO, accession code:
827 GSE109125). Samples used in the analysis are specified in Figure S2A. PCA and gene set analysis
828 was performed similar to that of the scRNAseq data. Briefly, normalized counts were used as input
829 for the PCA. Genes were ranked according to the leading vector of each PC and used as input for
830 the FGSEA algorithm along with KEGG and GO databases.

831 For the analysis of AMs, total RNA was isolated from CD45⁺ F4/80⁺ CD11c⁺ FACS-sorted cells
832 from the lung of 3 week-old *Tfam*^{ff} and *CD11c* Δ *Tfam* mice and subjected to RNAseq. Next
833 generation sequencing experiments were performed in the Genomics Unit of the CNIC on the
834 Illumina HiSeq 4000 System. Reads were mapped against reference transcriptome GRCm38.99,
835 quantified using RSEM using expected expression counts and normalized as previously indicated.
836 Genes were ranked according to log-Fold change and gene set enrichment analysis was performed
837 using FGSEA algorithm and KEGG and GO databases. Heatmaps display deregulated genes (Adj.
838 p-value ≤ 0.05) of the specified gene set.

839 ***GC-MS untargeted metabolomics***

840 Samples were prepared for the gas chromatography and mass spectrometry (GC-MS) untargeted
841 metabolomics analysis by optimizing methods previously described (Mastrangelo et al., 2016).
842 Briefly, 1mL of cold MeOH:H₂O (9:1, v:v) was added to each sample containing 10⁶ CD45⁺
843 F4/80⁺ CD11c⁺ FACS-sorted AMs from the BAL of adult *Tfam*^{ff} and *CD11c* Δ *Tfam* mice. Samples
844 were subjected to two freeze–thaw cycles for metabolism quenching and complete metabolite
845 extraction, specifically by placing the samples at -80°C for 15 min and thawing them on ice for 10
846 min with brief vortex-mixing. The samples were then centrifuged at 20,000 xg at 4°C for 10 min
847 and the supernatant collected. The supernatant was evaporated to dryness (SpeedVac Concentrator,
848 Thermo Fisher Scientific, Waltham, MA, USA) and derivatized with 10 μ l O-methoxyamine
849 hydrochloride (15mg/mL) in pyridine and 10 μ l N,O-bis(trimethylsilyl)trifluoroacetamide in 1%
850 trimethylchlorosilane. Finally, 100 μ l of heptane containing 10 ppm of 4-nitrobenzoic acid (IS)
851 was used as internal standard to monitor sample injection. For data acquisition, 7250 GC/Q-TOF
852 using the electron ionization (EI) source was used; separation was carried out using a J&W guard
853 column (10 m x 0.25 mm, 0.25 μ m), integrated with a DB5-MS column (30 m x 0.25 mm, 0.25

854 μm film, Agilent Technologies). Metabolite deconvolution and identification were carried out
855 using Agilent MassHunter Unknowns Analysis version B.07.00, then, data was aligned in Agilent
856 Mass Profiler Professional version B.12.1 and exported to Agilent MassHunter Quantitative
857 Analysis version B.07.00. Metabolites were identified by comparing their retention time, retention
858 index and mass fragmentation patterns with those available in an in-house library including both
859 the NIST mass spectral database (version 2017) and Fiehn RTL library (version 2008). Samples
860 were normalized by IS as reference feature. The result was a matrix with the compounds in the
861 samples sorted by their characteristic retention time and target ion, and the relative abundance of
862 each compound for each sample.

863 Quality Control (QC) samples (n=4) were prepared by pooling equal volumes of cell extracts from
864 each sample by following protocols mentioned above. QC samples were injected at the beginning,
865 at the end and every six samples in order to assess the reproducibility of both sample preparation
866 and data acquisition. Raw data from all samples were processed as described above. Data quality
867 was assured by using the QC samples as reference by filtering the data matrix. Specifically,
868 metabolites present in 50% of the QC samples with a coefficient of variation below 50% were
869 retained and the resulting data matrix underwent principal component analysis (PCA) on
870 Metaboanalyst website (<http://www.metaboanalyst.ca/>) to assess the analytical reproducibility.
871 Cube root transformed metabolites' levels from knockout and wild type mice were compared using
872 Student's t test and the p-values adjusted using the Benjamini–Hochberg method correcting for
873 false discovery rate (FDR, $q=0.05$). Differences were considered statistically significant when
874 $p \leq 0.05$. Individual samples (n=3 per each genotype) were generated by merging FACS-sorted AMs
875 to 10^6 cells/sample from >10 independent experiments of more than 13-30 animals/genotype.

876 ***Nucleic acid analysis and quantitative PCR***

877 From FACS-sorted TMF cells, total DNA was isolated using the QIAamp DNA Mini Kit. Tissue
878 was homogenized using an IKA Ultra-Turrax T-10 disperser and total RNA of tissue and TMFs
879 was extracted with the RNeasy Micro or Mini Kit and reverse transcribed using the High Capacity
880 cDNA Reverse Transcription Kit with random hexamers following manufacturer's instructions.
881 Quantitative PCR was performed using the GoTaq® qPCR Master Mix in a 7900HT Fast Real-
882 Time PCR System (Applied Biosystem®). Please find all sequences of primers used in Table S1
883 in the supplementary information. $2^{-\Delta\text{Ct}}$ mRNA expression values of mouse genes were calculated
884 relative to expression of *18S rRNA* and *mt-Co2* (mt-DNA) levels were calculated relative to *Sdh*
885 (nuclear DNA). For detection of *Xbp1* splice isoforms, the PCR product was purified using the
886 MinElute PCR Purification Kit and digested with the PstI-High-Fidelity restriction enzyme for 60
887 min at 37°C . Then, DNA bands were separated by agarose gel electrophoresis and imaged
888 following standard procedures and quantified using ImageJ/Fiji (Han et al., 2009).

889 ***In vitro treatments and lactate measurement***

890 10^5 MACS-purified BAL-AMs from pools of 3 week-old mice were analyzed directly or cultured
891 for 48 hours before staining and mRNA extraction. $0.2-1 \times 10^5$ MACS-purified BAL-AMs from
892 pools of adult mice were cultured for 6 hours or 24 hours, respectively, under presence or not of
893 PERK inhibitor GSK2606414, LXR agonists $1 \mu\text{M}$ T0901317 or $0.1 \mu\text{M}$ GW3965 before extraction
894 of mRNA. 3×10^5 MACS-purified BAL-AMs from pools of adult mice were cultured for 3 days to
895 collect supernatant for lactate measurement using the colorimetric Lactate Assay Kit following
896 manufacturers' instructions.

897 ***Analysis of proteinosis***

898 A vein catheter (BD) was inserted into the trachea and the first wash was performed with PBS
899 following 2-9 washes with 0.3-1 ml FACS buffer to harvest BAL cells. The first BAL-wash with
900 PBS was centrifuged for 5min at 500 xg and the supernatant used for measurement of optical
901 density at 600 nm using a spectral photometer (after a 1:3 dilution). Protein levels were determined
902 with the Pierce™ BCA Protein Assay Kit and total cholesterol levels using the Cholesterol
903 Quantitation Kit according to manufacturers' instructions. The cell pellet was merged with the rest
904 of the BAL washes for determination of cell debris and cell analysis by flow cytometry.

905 ***[1-¹⁴C]-Palmitate oxidation***

906 Measurement of FA oxidation rates was performed as previously described (Huynh et al., 2014).
907 1.5×10^5 MACS-purified BAL-AMs from pools of adult mice were seeded onto Fibronectin-coated
908 48 well plates and cultured in R10 overnight. Then, AMs were incubated in 500 μ l of media
909 containing 0.3% BSA/100 μ M palmitate/1 mM L-Carnitine/0.4 μ Ci/ml ¹⁴C-palmitate at 37°C for
910 3 hours. Each sample was assayed in duplicate. The reaction was stopped by the addition of 200
911 μ l of 1 M perchloric acid. The rate of palmitate oxidation was measured as released ¹⁴CO₂ trapped
912 in a filter paper disk with 20 μ l of 1 M NaOH on the top of sealed vials. ¹⁴C products were counted
913 in an LS6500 liquid scintillation counter (Beckman Coulter). Scintillation values were converted
914 to nmol ¹⁴CO₂ by multiplying the specific activity and normalized to DNA content (determined
915 with the CyQUANT NF Cell Proliferation Assay Kit following the manufacturers' instructions).

916 ***Metabolic flux analysis***

917 For metabolic flux analysis (Mitostress test), 1.25×10^5 MACS-purified BAL-AMs from pools of
918 adult mice were plated per well onto Fibronectin-coated Seahorse plates (Agilent Technologies,
919 Seahorse Bioscience) and cultured in R10 overnight before changing to Seahorse media [DMEM
920 (Gibco) supplemented with 100 U/mL Penicillin and Streptomycin and either 2 mM L-Glutamine,
921 1 mM Sodium Pyruvate and 25 mM Glucose or 5 mM L-Carnitine and 50 μ M Palmitoyl-CoA (all
922 Sigma) at pH 7.4] and incubation at 37°C without CO₂ for 30 min. Real-time oxygen-consumption
923 rate (OCR) and extracellular acidification rate (ECAR) in AMs were determined with an XF-96
924 Extracellular Flux Analyzer (Agilent Technologies, Seahorse Bioscience). Three measurements
925 were performed at the basal state and, for some experiments, after the sequential addition of the
926 following inhibitors every 15 min (Mito-stress test): 1 μ M Oligomycin, 1 μ M Carbonyl cyanide 3-
927 chlorophenylhydrazone (CCCP), and 1 μ M Rotenone with 1 μ M Antimycin A. Basal respiratory
928 rate (BRR), maximal respiratory rate (MRR), spare respiratory capacity (SRC), respiration linked
929 to mitochondrial ATP (mt-ATP) production and ECAR were calculated according to
930 manufacturers' instructions.

931 ***ATP measurements***

932 $1-5 \times 10^4$ FACS-sorted TMF cells were incubated or not for 10 min at RT with 10 mM 2-deoxy-D-
933 glucose in PBS. Intracellular ATP content was determined using the Luminescent ATP Detection
934 Assay Kit following the manufacturers' instructions.

935 ***Cholesterol uptake and efflux measurements***

936 10^5 MACS-purified BAL-AMs from pools of adult mice were allowed to adhere in 100 μ l R10
937 medium overnight. Then, measurement of cholesterol uptake and efflux was performed using the
938 Cholesterol Efflux Assay Kit with the acceptor Lipoprotein (High Density from human plasma,
939 solution) according to the manufacturers' instructions.

940 ***Fluorescence microscopy***

941 MACS-purified BAL-AMs from pools of 3 week-old or adult mice were allowed to adhere
942 overnight in R10 media on Fibronectin-coated μ -Slide 8 wells. Then, cells were incubated with
943 250 nM Tetramethylrhodamine methyl ester (TMRM), 100 nM MitoTracker™ Green FM and
944 APC-conjugated anti-CD11c antibody for 30 minutes in a humidified incubator at 37°C in staining
945 medium [RPMI without phenol red (Gibco), supplemented with 100 U/mL Penicillin and
946 Streptomycin, 2 mM L-Glutamine, 1 mM Sodium Pyruvate, 25 mM Glucose, 50 μ M β -
947 Mercaptoethanol (Sigma), 0.1 mM NEAA, and 1 mM HEPES (both from HyClone™)]. Hoechst
948 33342 dye was added for 5 minutes, cells washed and immediately imaged in staining media
949 containing 25 nM TMRM with the Nikon A1R confocal microscope (60x objective). Alive cells
950 were kept at 37°C at all times. Automatic image analysis was carried out with ImageJ/Fiji and cell
951 area was determined using CD11c staining area and positive TMRM or MitoTracker Green pixels
952 were quantified within each cell.

953 Alternatively, AMs were seeded onto Fibronectin-coated class coverslips and cultured overnight
954 in R10 media. Then, cells were stained with 1 μ g/ml Nile-Red in PBS for 30 min at RT, fixed for
955 20 min with 4% paraformaldehyde (PFA, Sigma) and incubated with DAPI for 10 min. For
956 epidermal ear sheet preparations, skin layers of ears from adult mice were separated using tweezers
957 and incubated floating on 3.8% ammonium thiocyanate (Sigma)/PBS for 25 min at 37°C. Then,
958 epidermis was carefully separated from the dermis and fixed in 4% PFA floating on PBS for 30
959 min at RT. Epidermal sheets were blocked with 2% BSA in PBS for 2 h at RT, incubated with
960 Langerin-Alexa Fluor 488 antibody (clone 929F3.01) at 4°C overnight and stained with DAPI for
961 20 min at RT. After mounting with ProLong™ Gold Antifade mounting media, AMs or epidermal
962 sheets were imaged using the Nikon ECLIPSE Ti-TimeLapse microscope and Langerin⁺ cells,
963 which mark Langerhans cells in the epidermis, quantified using ImageJ/Fiji software.

964 ***Transmission electron microscopy***

965 Pellets of CD45⁺ F4/80⁺ CD11c⁺ FACS-sorted AMs from the BAL of adult *Tfam*^{ff} and
966 *CD11c Δ Tfam* mice were fixed for 4 hours at 4°C in 0.1 M cacodylate buffer with 5% PFA and 4%
967 glutaraldehyde, washed 3 times with PBS and incubated in 1% osmium tetroxide for 1 hour. Then,
968 samples were treated for 10 min with 0.5% uranyl acetate and dehydrated with increasing
969 concentrations of ethanol and acetate before the infiltration with epoxy resin Durcupan™ (all
970 Sigma). After polymerization, 60 nm sections were cut using an ultra-microtome (Leica Reichert
971 ultracut), contrast-stained with 2% uranyl acetate and Reynold's lead and imaged using a
972 transmission electron microscope [Jeol Jem 1010 (Japan)] equipped with a digital camera [Gatan
973 Orius 200 SC (Pleasanton-CA)].

974 ***Histology and image analysis***

975 Adipose and liver tissue samples were fixed in 10% formalin (Sigma) for 48 hours, processed and
976 embedded in paraffin. Sections (5 μ m) were prepared and mounted on slides for staining with
977 hematoxylin and eosin (Sigma-Aldrich and Thermo Scientific) or immunohistochemistry.
978 Immunohistochemistry was performed using the primary rat monoclonal anti-F4/80 antibody
979 (Abcam ab6640, clone A3-1) and secondary antibodies HRP-conjugated rabbit anti-rat antibody
980 (Agilent P045001) and HRP-conjugated goat anti-rabbit polymer (EnVision® K4003, Agilent).
981 DAB (3,3'-diaminobenzidine) was used for visualization and nuclei were counterstained with
982 hematoxylin. All the immunohistochemical procedures were performed using an automated
983 autostainer (Autostainer Plus®, Dako). Alternatively, liver tissue samples were rehydrated in 30%
984 sucrose (Sigma) for 3 days and embedded in OCT compound (Tissue-Tek). Sections (8 μ m) were
985 stained with Oil red-O stain (American Master Tech Scientific, 0.7% in propylene glycol) for lipid
986 staining.

987 For lipid content, crown-like structures (CLS) and adipocyte size quantification, slides were
988 digitalized, analyzed with NDP.view2 viewing (Hamamatsu), and quantified with ImageJ/Fiji
989 software to evaluate the Oil red-O-positive area versus the total area (manual quantification). CLS
990 per field-of-view were counted manually. Adipocyte size was automatically quantified with
991 ImageJ/Fiji software using the Cellpose (Stringer et al., 2021) algorithm for cellular segmentation.

992 ***Blood and plasma analysis***

993 Blood was collected by bleeding from the submaxillary vein or cardiac puncture in EDTA-
994 containing tubes (Sarstedt) and white blood cell (WBC) count determined immediately using an
995 ABX Pentra XL 80 (HORIBA Medical). Plasma was obtained by centrifugation at 1000 xg for 30
996 min at 4°C and snap-frozen in liquid nitrogen. Plasma enzymes or biochemical parameters
997 (ALT/GPT, total cholesterol, free cholesterol, HDL, LDL and triglycerides) were analyzed with a
998 Dimension RxL Max automated analyzer.

999 **QUANTIFICATION AND STATISTICAL ANALYSIS**

1000 Data analyses employed GraphPad Prism version 7.0c. Data are presented as mean ± standard error
1001 of the mean or individual values and were analyzed as indicated in the legends or the dedicated
1002 methods section. All experiments were repeated at least twice and pooled data from several
1003 experiments are shown as indicated in the legends. Mice were allocated randomly in different
1004 experimental groups, but no blinding or randomization strategy was used. No animals were
1005 excluded from analysis, unless they had wounds from fighting/over-grooming. All n values
1006 represent biological replicates (different mice, primary cell preparations or in vitro experiments).
1007 Differences were considered significant when $P \leq 0.05$ and are indicated as ns, not significant, * P
1008 ≤ 0.05 , ** $P \leq 0.01$, *** $P \leq 0.001$.

References

- Acín-Pérez, R., Iborra, S., Martí-Mateos, Y., Cook, E.C.L., Conde-Garrosa, R., Petcherski, A., Muñoz, M. ^aM, Martínez de Mena, R., Krishnan, K.C., Jiménez, C., et al. (2020). Fgr kinase is required for proinflammatory macrophage activation during diet-induced obesity. *Nat. Metab.* *2*, 974–988. <https://doi.org/10.1038/s42255-020-00273-8>.
- Amano, S.U., Cohen, J.L., Vangala, P., Tencerova, M., Nicoloso, S.M., Yawe, J.C., Shen, Y., Czech, M.P., and Aouadi, M. (2014). Local proliferation of macrophages contributes to obesity-associated adipose tissue inflammation. *Cell Metab.* *19*, 162–171. <https://doi.org/10.1016/j.cmet.2013.11.017>.
- Bae, C., Hino, J., Hosoda, H., Son, C., Makino, H., Tokudome, T., Tomita, T., Hosoda, K., Miyazato, M., and Kangawa, K. (2018). Adipocyte-specific expression of C-type natriuretic peptide suppresses lipid metabolism and adipocyte hypertrophy in adipose tissues in mice fed high-fat diet. *Sci. Rep.* *8*, 2093. <https://doi.org/10.1038/s41598-018-20469-z>.
- Baixauli, F., Acín-Pérez, R., Villarroya-Beltrí, C., Mazzeo, C., Nuñez-Andrade, N., Gabandé-Rodríguez, E., Ledesma, M.D., Blázquez, A., Martín, M.A., Falcón-Pérez, J.M., et al. (2015). Mitochondrial Respiration Controls Lysosomal Function during Inflammatory T Cell Responses. *Cell Metab.* *22*, 485–498. <https://doi.org/10.1016/j.cmet.2015.07.020>.
- Botas, C., Poulain, F., Akiyama, J., Brown, C., Allen, L., Goerke, J., Clements, J., Carlson, E., Gillespie, A.M., Epstein, C., et al. (1998). Altered surfactant homeostasis and alveolar type II cell morphology in mice lacking surfactant protein D. *Proc. Natl. Acad. Sci. U. S. A.* *95*, 11869–11874. <https://doi.org/10.1073/pnas.95.20.11869>.
- Boutens, L., Hooiveld, G.J., Dhingra, S., Cramer, R.A., Netea, M.G., and Stienstra, R. (2018). Unique metabolic activation of adipose tissue macrophages in obesity promotes inflammatory responses. *Diabetologia* *61*, 942–953. <https://doi.org/10.1007/s00125-017-4526-6>.
- Butler, A., Hoffman, P., Smibert, P., Papalex, E., and Satija, R. (2018). Integrating single-cell transcriptomic data across different conditions, technologies, and species. *Nat. Biotechnol.* *36*, 411–420. <https://doi.org/10.1038/nbt.4096>.
- Caputa, G., Castoldi, A., and Pearce, E.J. (2019). Metabolic adaptations of tissue-resident immune cells. *Nat. Immunol.* *20*, 793–801. <https://doi.org/10.1038/s41590-019-0407-0>.
- Cardaci, S., Zheng, L., MacKay, G., van den Broek, N.J.F., MacKenzie, E.D., Nixon, C., Stevenson, D., Tumanov, S., Bulusu, V., Kamphorst, J.J., et al. (2015). Pyruvate carboxylation enables growth of SDH-deficient cells by supporting aspartate biosynthesis. *Nat. Cell Biol.* *17*, 1317–1326. <https://doi.org/10.1038/ncb3233>.
- Caton, M.L., Smith-Raska, M.R., and Reizis, B. (2007). Notch–RBP–J signaling controls the homeostasis of CD8– dendritic cells in the spleen. *J. Exp. Med.* *204*, 1653–1664. <https://doi.org/10.1084/jem.20062648>.
- Chokchaiwong, S., Kuo, Y., Lin, S., Hsu, Y.-C., Hsu, S., Liu, Y., Chou, A., and Kao, S. (2018). Coenzyme Q10 serves to couple mitochondrial oxidative phosphorylation and fatty acid β -oxidation, and attenuates NLRP3 inflammasome activation. *Free Radic. Res.* *52*, 1445–1455. <https://doi.org/10.1080/10715762.2018.1500695>.
- Clausen, B.E., Burkhardt, C., Reith, W., Renkawitz, R., and Förster, I. (1999). Conditional gene targeting in macrophages and granulocytes using LysMcre mice. *Transgenic Res.* *8*, 265–277. <https://doi.org/10.1023/a:1008942828960>.
- Dahik, V.D., Frisdal, E., and Le Goff, W. (2020). Rewiring of Lipid Metabolism in Adipose Tissue Macrophages in Obesity: Impact on Insulin Resistance and Type 2 Diabetes. *Int. J. Mol. Sci.* *21*, 1–30. <https://doi.org/10.3390/ijms21155505>.
- Davies, L.C., Rice, C.M., Palmieri, E.M., Taylor, P.R., Kuhns, D.B., and McVicar, D.W. (2017).

1056 Peritoneal tissue-resident macrophages are metabolically poised to engage microbes using
1057 tissue-niche fuels. *Nat. Commun.* 8, 2074. <https://doi.org/10.1038/s41467-017-02092-0>.

1058 Desdín-Micó, G., Soto-Herederó, G., Aranda, J.F., Oller, J., Carrasco, E., Gabandé-Rodríguez,
1059 E., Blanco, E.M., Alfranca, A., Cussó, L., Desco, M., et al. (2020). T cells with dysfunctional
1060 mitochondria induce multimorbidity and premature senescence. *Science*. 368, 1371–1376.
1061 <https://doi.org/10.1126/science.aax0860>.

1062 Diaz, F., Thomas, C.K., Garcia, S., Hernandez, D., and Moraes, C.T. (2005). Mice lacking
1063 COX10 in skeletal muscle recapitulate the phenotype of progressive mitochondrial
1064 myopathies associated with cytochrome c oxidase deficiency. *Hum. Mol. Genet.* 14, 2737–
1065 2748. <https://doi.org/10.1093/hmg/ddi307>.

1066 Faas, M., Ipseiz, N., Ackermann, J., Culemann, S., Grüneboom, A., Schröder, F., Rothe, T.,
1067 Scholtysek, C., Eberhardt, M., Böttcher, M., et al. (2021). IL-33-induced metabolic
1068 reprogramming controls the differentiation of alternatively activated macrophages and the
1069 resolution of inflammation. *Immunity* 54, 2531-2546.e5.
1070 <https://doi.org/10.1016/j.immuni.2021.09.010>.

1071 Feng, B., Yao, P.M., Li, Y., Devlin, C.M., Zhang, D., Harding, H.P., Sweeney, M., Rong, J.X.,
1072 Kuriakose, G., Fisher, E.A., et al. (2003). The endoplasmic reticulum is the site of cholesterol-
1073 induced cytotoxicity in macrophages. *Nat. Cell Biol.* 5, 781–792.
1074 <https://doi.org/10.1038/ncb1035>.

1075 Fessler, M.B., and Summer, R.S. (2016). Surfactant lipids at the host-environment interface
1076 metabolic sensors, suppressors, and effectors of inflammatory lung disease. *Am. J. Respir.*
1077 *Cell Mol. Biol.* 54, 624–635. <https://doi.org/10.1165/rcmb.2016-0011PS>.

1078 Fessler, E., Eckl, E., Schmitt, S., Mancilla, I.A., Meyer-Bender, M.F., Hanf, M., Philippou-
1079 Massier, J., Krebs, S., Zischka, H., and Jae, L.T. (2020). A pathway coordinated by DELE1
1080 relays mitochondrial stress to the cytosol. *Nature* 579, 433–437.
1081 <https://doi.org/10.1038/s41586-020-2076-4>.

1082 Fu, X., Menke, J.G., Chen, Y., Zhou, G., MacNaul, K.L., Wright, S.D., Sparrow, C.P., and Lund,
1083 E.G. (2001). 27-hydroxycholesterol is an endogenous ligand for liver X receptor in
1084 cholesterol-loaded cells. *J. Biol. Chem.* 276, 38378–38387.
1085 <https://doi.org/10.1074/jbc.M105805200>.

1086 Gao, X., Zhu, B., Wu, Y., Li, C., Zhou, X., Tang, J., and Sun, J. (2022). TFAM-Dependent
1087 Mitochondrial Metabolism Is Required for Alveolar Macrophage Maintenance and
1088 Homeostasis. *J. Immunol.* 208, 1456–1466. <https://doi.org/10.4049/jimmunol.2100741>.

1089 Garaude, J., Acín-Pérez, R., Martínez-Cano, S., Enamorado, M., Ugolini, M., Nistal-Villán, E.,
1090 Hervás-Stubbs, S., Pelegrín, P., Sander, L.E., Enríquez, J.A., et al. (2016). Mitochondrial
1091 respiratory-chain adaptations in macrophages contribute to antibacterial host defense. *Nat.*
1092 *Immunol.* 17, 1037–1045. <https://doi.org/10.1038/ni.3509>.

1093 Graham, A. (2015). Mitochondrial regulation of macrophage cholesterol homeostasis. *Free*
1094 *Radic. Biol. Med.* 89, 982–992. <https://doi.org/10.1016/j.freeradbiomed.2015.08.010>.

1095 Guo, X., Aviles, G., Liu, Y., Tian, R., Unger, B.A., Lin, Y.-H.T., Wiita, A.P., Xu, K., Correia,
1096 M.A., and Kampmann, M. (2020). Mitochondrial stress is relayed to the cytosol by an
1097 OMA1-DELE1-HRI pathway. *Nature* 579, 427–432. <https://doi.org/10.1038/s41586-020-2078-2>.

1099 Han, D., Lerner, A.G., Vande Walle, L., Upton, J., Xu, W., Hagen, A., Backes, B.J., Oakes, S.A.,
1100 and Papa, F.R. (2009). IRE1alpha kinase activation modes control alternate endoribonuclease
1101 outputs to determine divergent cell fates. *Cell* 138, 562–575.
1102 <https://doi.org/10.1016/j.cell.2009.07.017>.

1103 Han, X., Zhou, Z., Fei, L., Sun, H., Wang, R., Chen, Y., Chen, H., Wang, J., Tang, H., Ge, W., et
1104 al. (2020). Construction of a human cell landscape at single-cell level. *Nature* 581, 303–309.
1105 <https://doi.org/10.1038/s41586-020-2157-4>.

1106 Hernández-García, E., Cueto, F.J., Cook, E.C.L., Redondo-Urzainqui, A., Charro-Zanca, S.,
1107 Robles-Vera, I., Conde-Garrosa, R., Nikolić, I., Sabio, G., Sancho, D., et al. (2022).
1108 Conventional type 1 dendritic cells protect against age-related adipose tissue dysfunction and
1109 obesity. *Cell. Mol. Immunol.* 19, 260–275. <https://doi.org/10.1038/s41423-021-00812-7>.

1110 Hill, D.A., Lim, H.W., Kim, Y.H., Ho, W.Y., Foong, Y.H., Nelson, V.L., Nguyen, H.C.B.,
1111 Chegireddy, K., Kim, J., Habberthuer, A., et al. (2018). Distinct macrophage populations
1112 direct inflammatory versus physiological changes in adipose tissue. *Proc. Natl. Acad. Sci. U.*
1113 *S. A.* 115, E5096–E5105. <https://doi.org/10.1073/pnas.1802611115>.

1114 Huber, W., Carey, V.J., Gentleman, R., Anders, S., Carlson, M., Carvalho, B.S., Bravo, H.C.,
1115 Davis, S., Gatto, L., Girke, T., et al. (2015). Orchestrating high-throughput genomic analysis
1116 with Bioconductor. *Nat. Methods* 12, 115–121. <https://doi.org/10.1038/nmeth.3252>.

1117 Huynh, F.K., Green, M.F., Koves, T.R., and Hirschey, M.D. (2014). Measurement of fatty acid
1118 oxidation rates in animal tissues and cell lines. *Methods Enzymol.* 542, 391–405.
1119 <https://doi.org/10.1016/B978-0-12-416618-9.00020-0>.

1120 Izquierdo, H.M., Brandi, P., Gómez, M.J., Conde-Garrosa, R., Priego, E., Enamorado, M.,
1121 Martínez-Cano, S., Sánchez, I., Conejero, L., Jimenez-Carretero, D., et al. (2018). Von
1122 Hippel-Lindau Protein Is Required for Optimal Alveolar Macrophage Terminal
1123 Differentiation, Self-Renewal, and Function. *Cell Rep.* 24, 1738–1746.
1124 <https://doi.org/10.1016/j.celrep.2018.07.034>.

1125 Jin, Z., Wei, W., Yang, M., Du, Y., and Wan, Y. (2014). Mitochondrial complex I activity
1126 suppresses inflammation and enhances bone resorption by shifting macrophage-osteoclast
1127 polarization. *Cell Metab.* 20, 483–498. <https://doi.org/10.1016/j.cmet.2014.07.011>.

1128 Karunakaran, D., Thrush, A.B., Nguyen, M.A., Richards, L., Geoffrion, M., Singaravelu, R.,
1129 Ramphos, E., Shangari, P., Ouimet, M., Pezacki, J.P., et al. (2015). Macrophage
1130 Mitochondrial Energy Status Regulates Cholesterol Efflux and Is Enhanced by Anti-miR33 in
1131 Atherosclerosis. *Circ. Res.* 117, 266–278.
1132 <https://doi.org/10.1161/CIRCRESAHA.117.305624>.

1133 Korf, H., Boesch, M., Meelberghs, L., and van der Merwe, S. (2019). Macrophages as Key
1134 Players during Adipose Tissue-Liver Crosstalk in Nonalcoholic Fatty Liver Disease. *Semin.*
1135 *Liver Dis.* 39, 291–300. <https://doi.org/10.1055/s-0039-1687851>.

1136 Kruse, S.E., Watt, W.C., Marcinek, D.J., Kapur, R.P., Schenkman, K.A., and Palmiter, R.D.
1137 (2008). Mice with Mitochondrial Complex I Deficiency Develop a Fatal Encephalomyopathy.
1138 *Cell Metab.* 7, 312–320. <https://doi.org/10.1016/j.cmet.2008.02.004>.

1139 Larsson, N.-G., Wang, J., Wilhelmsson, H., Oldfors, A., Rustin, P., Lewandoski, M., Barsh,
1140 G.S., and Clayton, D.A. (1998). Mitochondrial transcription factor A is necessary for mtDNA
1141 maintenance and embryogenesis in mice. *Nat. Genet.* 18, 231–236.
1142 <https://doi.org/10.1038/ng0398-231>.

1143 Latorre-Pellicer, A., Lechuga-Vieco, A.V., Johnston, I.G., Hämäläinen, R.H., Pellico, J., Justo-
1144 Méndez, R., Fernández-Toro, J.M., Clavería, C., Guaras, A., Sierra, R., et al. (2019).
1145 Regulation of Mother-to-Offspring Transmission of mtDNA Heteroplasmy. *Cell Metab.* 30,
1146 1120–1130.e5. <https://doi.org/10.1016/j.cmet.2019.09.007>.

1147 Lauterbach, M.A., Hanke, J.E., Serefidou, M., Mangan, M.S.J., Kolbe, C.-C., Hess, T., Rothe,
1148 M., Kaiser, R., Hoss, F., Gehlen, J., et al. (2019). Toll-like Receptor Signaling Rewires
1149 Macrophage Metabolism and Promotes Histone Acetylation via ATP-Citrate Lyase. *Immunity*

1150 51, 997-1011.e7. <https://doi.org/10.1016/j.immuni.2019.11.009>.

1151 Lefere, S., and Tacke, F. (2019). Macrophages in obesity and non-alcoholic fatty liver disease:
1152 Crosstalk with metabolism. *JHEP Reports* 1, 30–43.
1153 <https://doi.org/10.1016/j.jhepr.2019.02.004>.

1154 Lewandoski, M., Wassarman, K.M., and Martin, G.R. (1997). Zp3-cre, a transgenic mouse line
1155 for the activation or inactivation of loxP-flanked target genes specifically in the female germ
1156 line. *Curr. Biol.* 7, 148–151. [https://doi.org/10.1016/s0960-9822\(06\)00059-5](https://doi.org/10.1016/s0960-9822(06)00059-5).

1157 Li, P., Lu, M., Nguyen, M.T.A., Bae, E.J., Chapman, J., Feng, D., Hawkins, M., Pessin, J.E.,
1158 Sears, D.D., Nguyen, A.K., et al. (2010). Functional heterogeneity of CD11c-positive adipose
1159 tissue macrophages in diet-induced obese mice. *J. Biol. Chem.* 285, 15333–15345.
1160 <https://doi.org/10.1074/jbc.M110.100263>.

1161 Luo, W., Friedman, M.S., Shedden, K., Hankenson, K.D., and Woolf, P.J. (2009). GAGE:
1162 generally applicable gene set enrichment for pathway analysis. *BMC Bioinformatics* 10, 161.
1163 <https://doi.org/10.1186/1471-2105-10-161>.

1164 Martínez-López, M., Iborra, S., Conde-Garrosa, R., Mastrangelo, A., Danne, C., Mann, E.R.,
1165 Reid, D.M., Gaboriau-Routhiau, V., Chaparro, M., Lorenzo, M.P., et al. (2019). Microbiota
1166 Sensing by Mincle-Syk Axis in Dendritic Cells Regulates Interleukin-17 and -22 Production
1167 and Promotes Intestinal Barrier Integrity. *Immunity* 50, 446-461.e9.
1168 <https://doi.org/10.1016/j.immuni.2018.12.020>.

1169 Martínez-Reyes, I., and Chandel, N.S. (2020). Mitochondrial TCA cycle metabolites control
1170 physiology and disease. *Nat. Commun.* 11, 102. <https://doi.org/10.1038/s41467-019-13668-3>.

1171 Mastrangelo, A., Panadero, M.I., Perez, L.M., Galvez, B.G., Garcia, A., Barbas, C., and Ruperez,
1172 F.J. (2016). New insight on obesity and adipose-derived stem cells using comprehensive
1173 metabolomics. *Biochem. J.* 473, 2187–2203. <https://doi.org/10.1042/BCJ20160241>.

1174 Matesanz, N., Nikolic, I., Leiva, M., Pulgarín-Alfaro, M., Santamans, A.M., Bernardo, E., Mora,
1175 A., Herrera-Melle, L., Rodríguez, E., Beiroa, D., et al. (2018). p38 α blocks brown adipose
1176 tissue thermogenesis through p38 δ inhibition. *PLoS Biol.* 16, e2004455.
1177 <https://doi.org/10.1371/journal.pbio.2004455>.

1178 McCarthy, C., Lee, E., Bridges, J.P., Sallese, A., Suzuki, T., Woods, J.C., Bartholmai, B.J.,
1179 Wang, T., Chalk, C., Carey, B.C., et al. (2018). Statin as a novel pharmacotherapy of
1180 pulmonary alveolar proteinosis. *Nat. Commun.* 9, 3127. <https://doi.org/10.1038/s41467-018-05491-z>.

1181

1182 Mills, E.L., Kelly, B., Logan, A., Costa, A.S.H., Varma, M., Bryant, C.E., Turlomousis, P.,
1183 Däbritz, J.H.M., Gottlieb, E., Latorre, I., et al. (2016). Succinate Dehydrogenase Supports
1184 Metabolic Repurposing of Mitochondria to Drive Inflammatory Macrophages. *Cell* 167, 457-
1185 470.e13. <https://doi.org/10.1016/j.cell.2016.08.064>.

1186 Morgan, P.K., Huynh, K., Pernes, G., Miotto, P.M., Mellett, N.A., Giles, C., Meikle, P.J.,
1187 Murphy, A.J., and Lancaster, G.I. (2021). Macrophage polarization state affects lipid
1188 composition and the channeling of exogenous fatty acids into endogenous lipid pools. *J. Biol.*
1189 *Chem.* 297, 101341. <https://doi.org/10.1016/j.jbc.2021.101341>.

1190 Nishitoh, H. (2012). CHOP is a multifunctional transcription factor in the ER stress response. *J.*
1191 *Biochem.* 151, 217–219. <https://doi.org/10.1093/jb/mvr143>.

1192 Nobs, S.P., and Kopf, M. (2021). Tissue-resident macrophages: guardians of organ homeostasis.
1193 *Trends Immunol.* 42, 495–507. <https://doi.org/10.1016/j.it.2021.04.007>.

1194 O'Neill, L.A.J., Kishton, R.J., and Rathmell, J. (2016). A guide to immunometabolism for
1195 immunologists. *Nat. Rev. Immunol.* 16, 553–565. <https://doi.org/10.1038/nri.2016.70>.

1196 Pakos-Zebrucka, K., Koryga, I., Mnich, K., Ljujic, M., Samali, A., and Gorman, A.M. (2016).

1197 The integrated stress response. *EMBO Rep.* 17, 1374–1395.
1198 <https://doi.org/10.15252/embr.201642195>.

1199 Raines, L.N., Zhao, H., Wang, Y., Chen, H.-Y., Gallart-Ayala, H., Hsueh, P.-C., Cao, W., Koh,
1200 Y., Alamonte-Loya, A., Liu, P.-S., et al. (2022). PERK is a critical metabolic hub for
1201 immunosuppressive function in macrophages. *Nat. Immunol.* 23, 431–445.
1202 <https://doi.org/10.1038/s41590-022-01145-x>.

1203 Rao, R.R., Long, J.Z., White, J.P., Svensson, K.J., Lou, J., Lokurkar, I., Jedrychowski, M.P.,
1204 Ruas, J.L., Wrann, C.D., Lo, J.C., et al. (2014). Meteorin-like is a hormone that regulates
1205 immune-adipose interactions to increase beige fat thermogenesis. *Cell* 157, 1279–1291.
1206 <https://doi.org/10.1016/j.cell.2014.03.065>.

1207 Remmerie, A., and Scott, C.L. (2018). Macrophages and lipid metabolism. *Cell. Immunol.* 330,
1208 27–42. <https://doi.org/10.1016/j.cellimm.2018.01.020>.

1209 Russell, D.G., Huang, L., and VanderVen, B.C. (2019). Immunometabolism at the interface
1210 between macrophages and pathogens. *Nat. Rev. Immunol.* 19, 291–304.
1211 <https://doi.org/10.1038/s41577-019-0124-9>.

1212 Schindelin, J., Arganda-Carreras, I., Frise, E., Kaynig, V., Longair, M., Pietzsch, T., Preibisch,
1213 S., Rueden, C., Saalfeld, S., Schmid, B., et al. (2012). Fiji: an open-source platform for
1214 biological-image analysis. *Nat. Methods* 9, 676–682. <https://doi.org/10.1038/nmeth.2019>.

1215 Schneider, C., Nobs, S.P., Kurrer, M., Rehrauer, H., Thiele, C., and Kopf, M. (2014). Induction
1216 of the nuclear receptor PPAR- γ 3 by the cytokine GM-CSF is critical for the differentiation of
1217 fetal monocytes into alveolar macrophages. *Nat. Immunol.* 15, 1026–1037.
1218 <https://doi.org/10.1038/ni.3005>.

1219 Schuster, G.U., Parini, P., Wang, L., Alberti, S., Steffensen, K.R., Hansson, G.K., Angelin, B.,
1220 and Gustafsson, J.Å. (2002). Accumulation of foam cells in liver X receptor-deficient mice.
1221 *Circulation* 106, 1147–1153. <https://doi.org/10.1161/01.CIR.0000026802.79202.96>.

1222 Serbulea, V., Upchurch, C.M., Schappe, M.S., Voigt, P., DeWeese, D.E., Desai, B.N., Meher,
1223 A.K., and Leitinger, N. (2018). Macrophage phenotype and bioenergetics are controlled by
1224 oxidized phospholipids identified in lean and obese adipose tissue. *Proc. Natl. Acad. Sci. U.*
1225 *S. A.* 115, E6254–E6263. <https://doi.org/10.1073/pnas.1800544115>.

1226 Smeitink, J., van den Heuvel, L., and DiMauro, S. (2001). The genetics and pathology of
1227 oxidative phosphorylation. *Nat. Rev. Genet.* 2, 342–352. <https://doi.org/10.1038/35072063>.

1228 Soberanes, S., Misharin, A. V., Jairaman, A., Morales-Nebreda, L., McQuattie-Pimentel, A.C.,
1229 Cho, T., Hamanaka, R.B., Meliton, A.Y., Reyfman, P.A., Walter, J.M., et al. (2019).
1230 Metformin Targets Mitochondrial Electron Transport to Reduce Air-Pollution-Induced
1231 Thrombosis. *Cell Metab.* 29, 335-347.e5. <https://doi.org/10.1016/j.cmet.2018.09.019>.

1232 Stringer, C., Wang, T., Michaelos, M., and Pachitariu, M. (2021). Cellpose: a generalist
1233 algorithm for cellular segmentation. *Nat. Methods* 18, 100–106.
1234 <https://doi.org/10.1038/s41592-020-01018-x>.

1235 Svedberg, F.R., Brown, S.L., Krauss, M.Z., Campbell, L., Sharpe, C., Clausen, M., Howell, G.J.,
1236 Clark, H., Madsen, J., Evans, C.M., et al. (2019). The lung environment controls alveolar
1237 macrophage metabolism and responsiveness in type 2 inflammation. *Nat. Immunol.* 20, 571–
1238 580. <https://doi.org/10.1038/s41590-019-0352-y>.

1239 Tabas, I. (2002). Consequences of cellular cholesterol accumulation: basic concepts and
1240 physiological implications. *J. Clin. Invest.* 110, 905–911. <https://doi.org/10.1172/JCI16452>.

1241 Thomassen, M.J., Barna, B.P., Malur, A.G., Bonfield, T.L., Farver, C.F., Malur, A., Dalrymple,
1242 H., Kavuru, M.S., and Febbraio, M. (2007). ABCG1 is deficient in alveolar macrophages of
1243 GM-CSF knockout mice and patients with pulmonary alveolar proteinosis. *J. Lipid Res.* 48,

1244 2762–2768. <https://doi.org/10.1194/jlr.P700022-JLR200>.

1245 Wculek, S.K., Dunphy, G., Heras-Murillo, I., Mastrangelo, A., and Sancho, D. (2022).

1246 Metabolism of tissue macrophages in homeostasis and pathology. *Cell. Mol. Immunol.* *19*,

1247 384–408. <https://doi.org/10.1038/s41423-021-00791-9>.

1248 Weinberg, S.E., Singer, B.D., Steinert, E.M., Martinez, C.A., Mehta, M.M., Martínez-Reyes, I.,

1249 Gao, P., Helmin, K.A., Abdala-Valencia, H., Sena, L.A., et al. (2019). Mitochondrial complex

1250 III is essential for suppressive function of regulatory T cells. *Nature* *565*, 495–499.

1251 <https://doi.org/10.1038/s41586-018-0846-z>.

1252 Woods, P.S., Kimmig, L.M., Meliton, A.Y., Sun, K.A., Tian, Y., O’Leary, E.M., Gökalp, G.A.,

1253 Hamanaka, R.B., and Mutlu, G.M. (2020). Tissue-Resident Alveolar Macrophages Do Not

1254 Rely on Glycolysis for LPS-induced Inflammation. *Am. J. Respir. Cell Mol. Biol.* *62*, 243–

1255 255. <https://doi.org/10.1165/rcmb.2019-0244OC>.

1256 Yang, S., Bossche, J. Van Den, and Ramalho, T. (2020). Macrophage Metabolism at the

1257 Crossroad of Metabolic Diseases and Cancer. *Immunometabolism* *2*, 1–26.

1258 <https://doi.org/10.20900/immunometab20200022>.

1259 Yao, S., Miao, C., Tian, H., Sang, H., Yang, N., Jiao, P., Han, J., Zong, C., and Qin, S. (2014).

1260 Endoplasmic reticulum stress promotes macrophage-derived foam cell formation by up-

1261 regulating cluster of differentiation 36 (CD36) expression. *J. Biol. Chem.* *289*, 4032–4042.

1262 <https://doi.org/10.1074/jbc.M113.524512>.

1263 Yoshida, H., Lareau, C.A., Ramirez, R.N., Rose, S.A., Maier, B., Wroblewska, A., Desland, F.,

1264 Chudnovskiy, A., Mortha, A., Dominguez, C., et al. (2019). The cis-Regulatory Atlas of the

1265 Mouse Immune System. *Cell* *176*, 897-912.e20. <https://doi.org/10.1016/j.cell.2018.12.036>.

1266 Zhang, S., Weinberg, S., DeBerge, M., Gainullina, A., Schipma, M., Kinchen, J.M., Ben-Sahra,

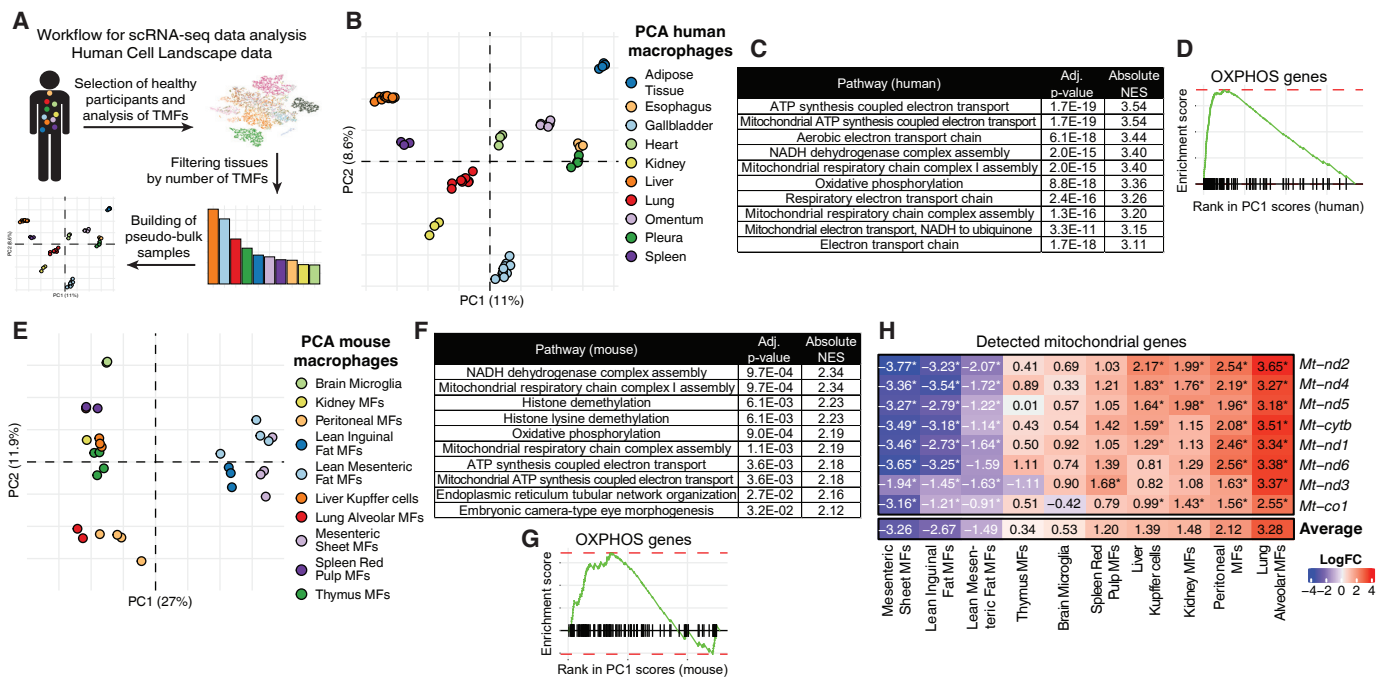
1267 I., Gius, D.R., Yvan-Charvet, L., Chandel, N.S., et al. (2019). Efferocytosis Fuels

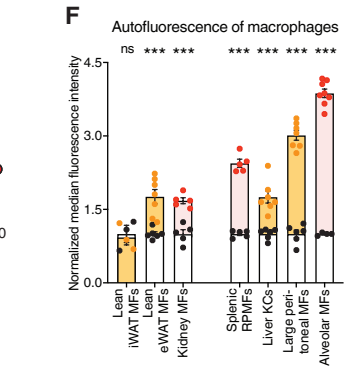
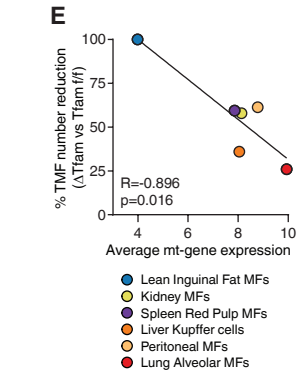
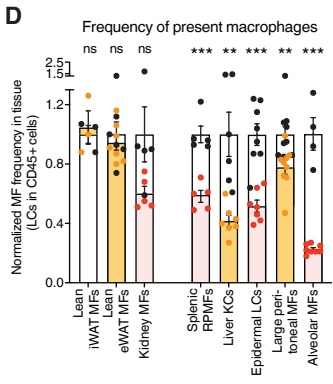
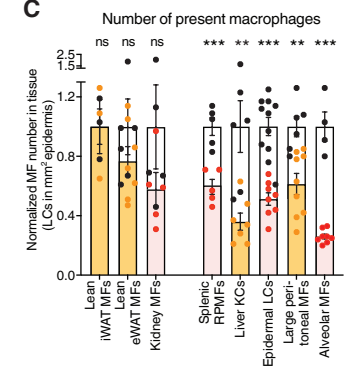
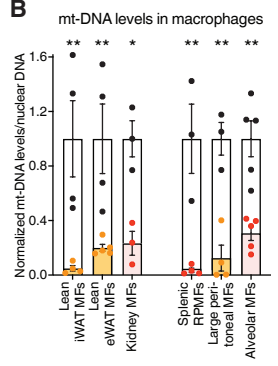
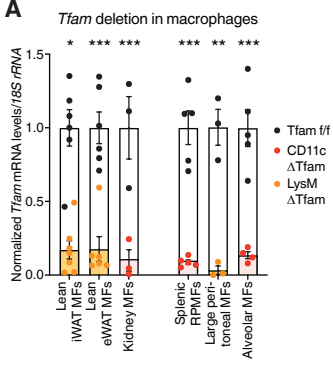
1268 Requirements of Fatty Acid Oxidation and the Electron Transport Chain to Polarize

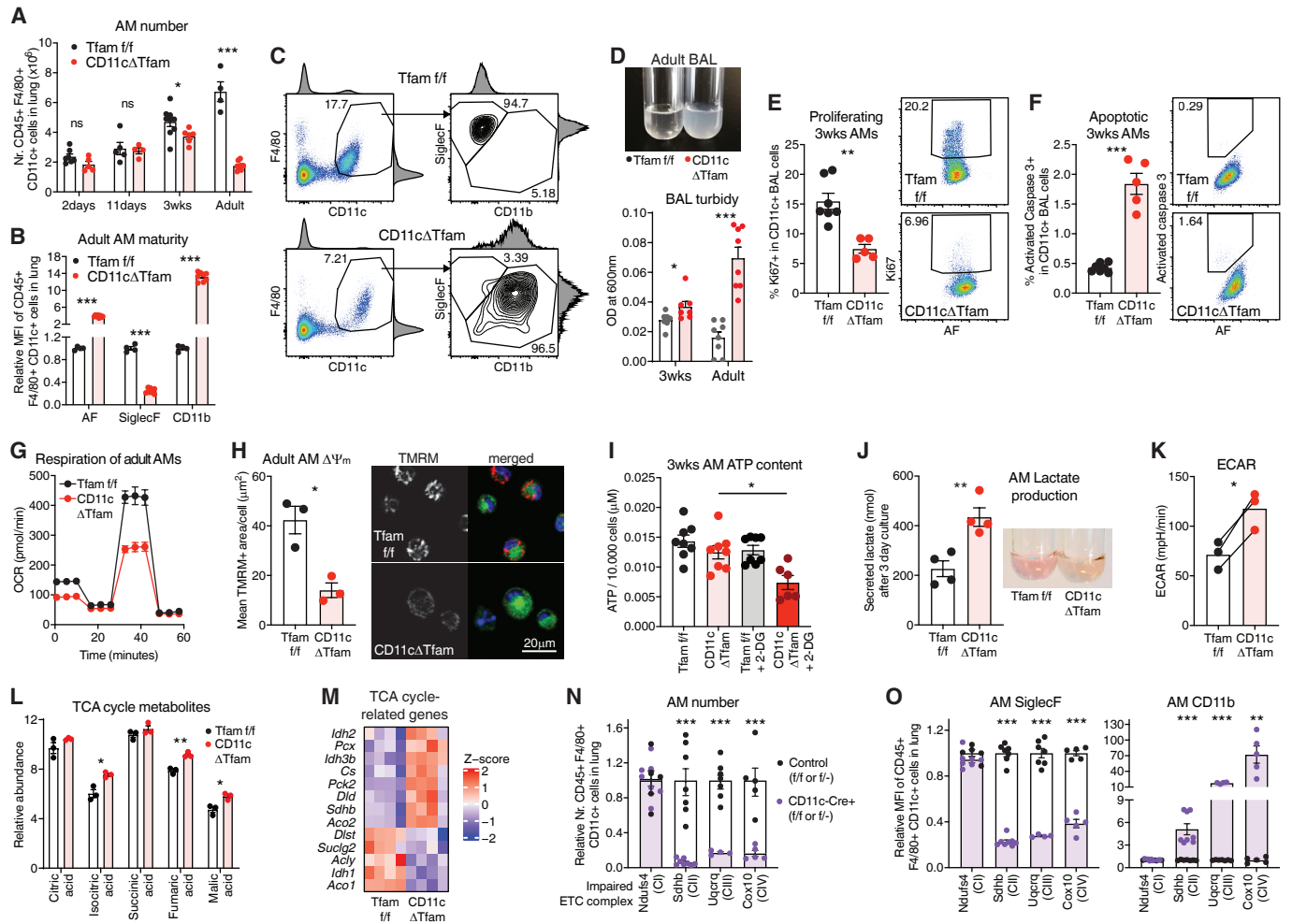
1269 Macrophages for Tissue Repair. *Cell Metab.* *29*, 443-456.e5.

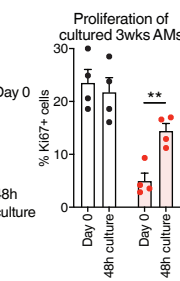
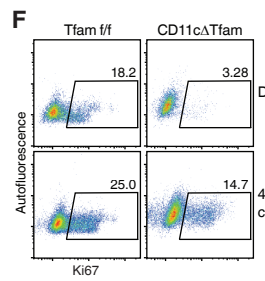
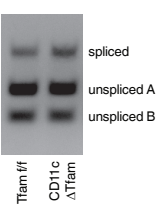
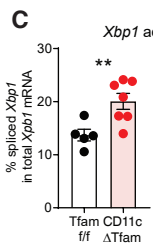
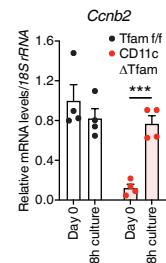
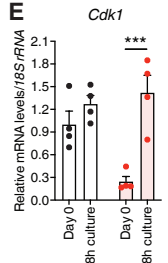
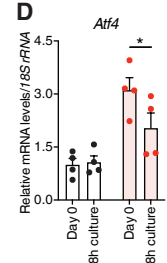
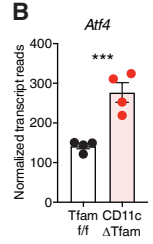
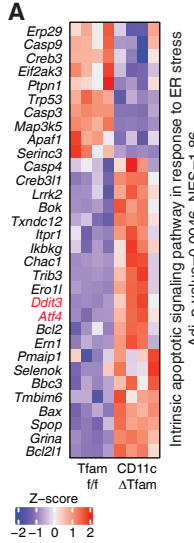
1270 <https://doi.org/10.1016/j.cmet.2018.12.004>.

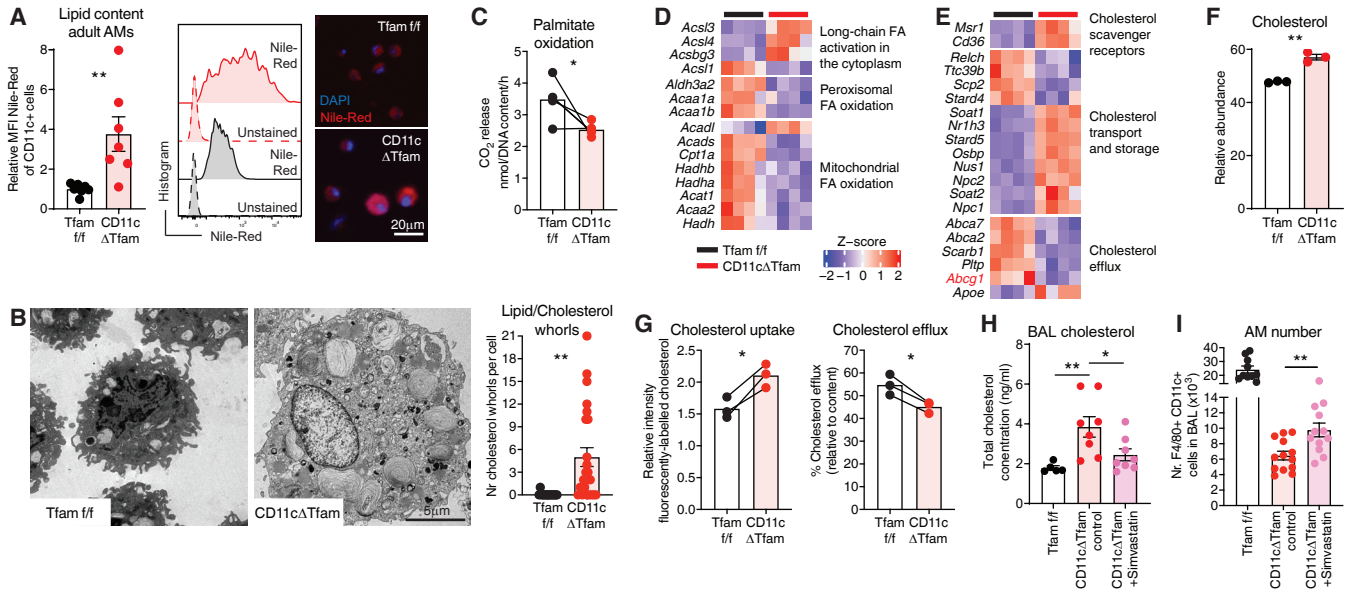
1271

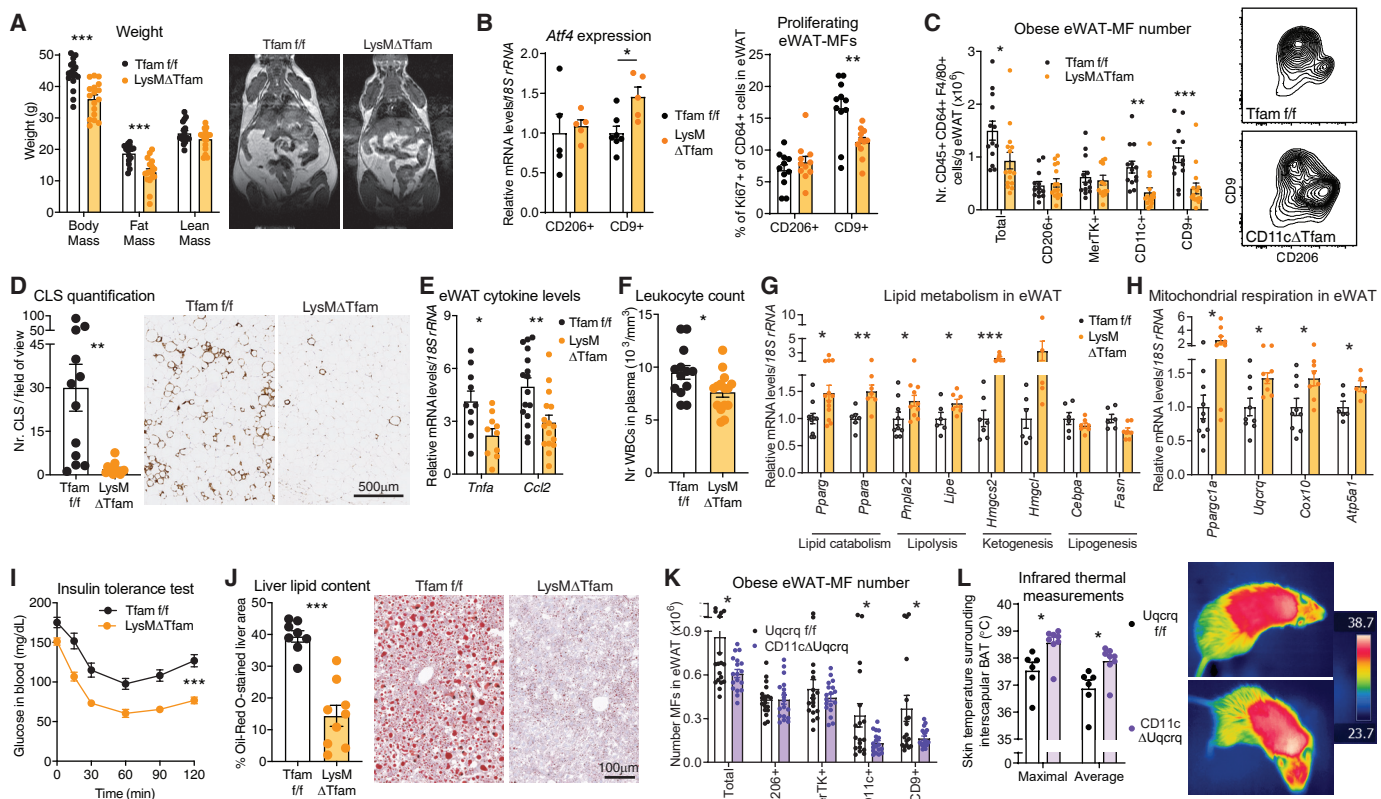












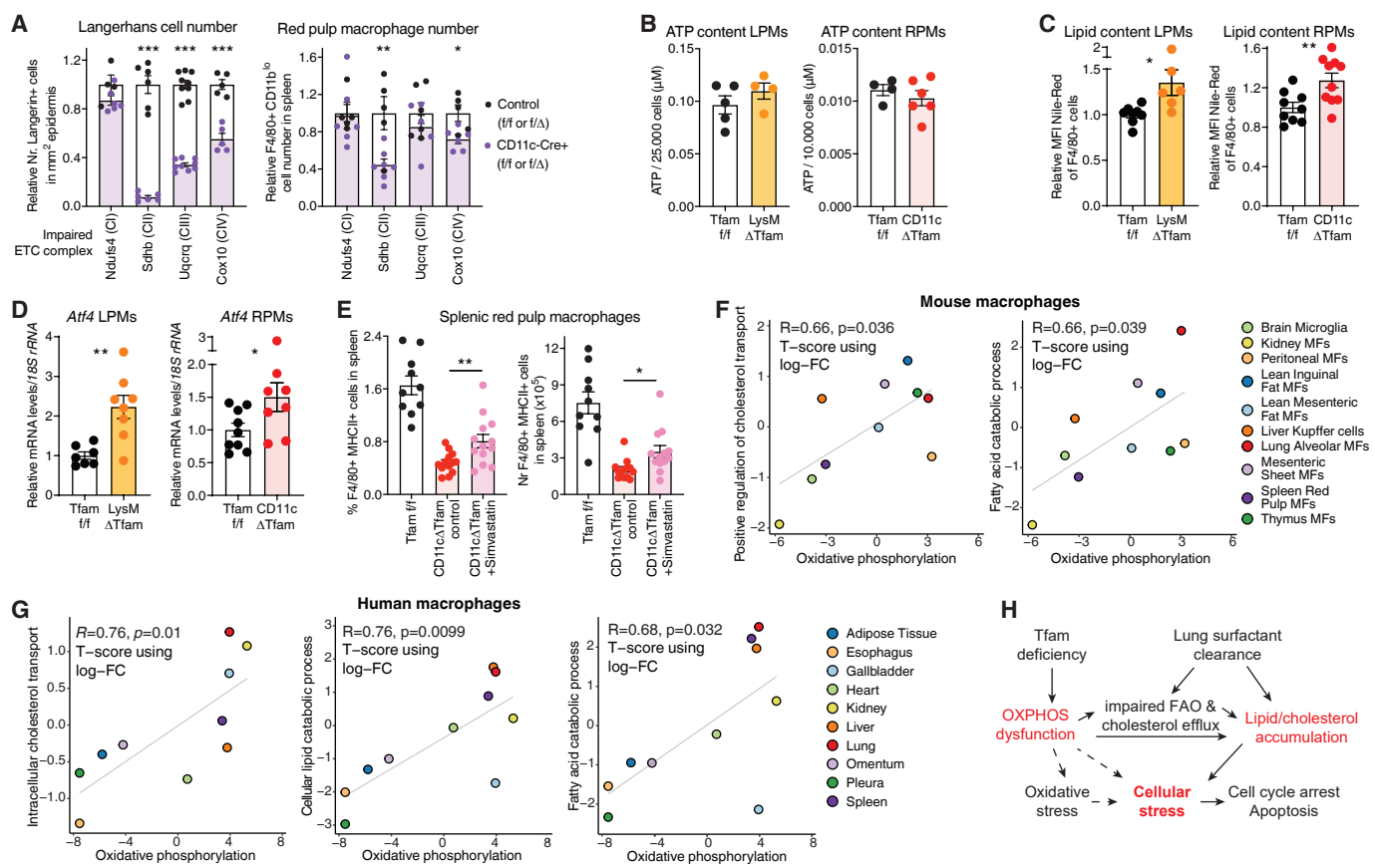


Table S1. Related to STAR methods and key resources table.

REAGENT or RESOURCE	SOURCE
Oligonucleotides	
qPCR <i>Tfam</i> sense (5')– CAGGAGGCAAAGGATGATTC–(3'), anti-sense (5')– CCAAGACTTCATTTTCATTGTCC–(3')	(Desdín-Micó et al., 2020)
qPCR <i>Slc2a1</i> sense (5')– GGGCATGTGCTTCCAGTATGT–(3'), anti-sense (5')– ACGAGGAGCACCGTGAAGAT–(3')	(Izquierdo et al., 2018)
qPCR <i>Atf4</i> sense (5')– ATGGCCGGCTATGGATGAT–(3'), anti-sense (5')– CGAAGTCAAACCTTTTCAGATCCATT–(3')	This paper
qPCR <i>Bax</i> sense (5')– CTACAGGGTTTCATCCAG–(3'), anti-sense (5')– CCAGTTCATCTCCAATTCG–(3')	This paper
qPCR <i>Cdk1</i> sense (5')– AGAAGGTAACCTACGGTGTGGT–(3'), anti-sense (5')– GAGAGATTTCCCGAATTGCAGT–(3')	(Izquierdo et al., 2018)
qPCR <i>Cnnb2</i> sense (5')– GCCAAGAGCCATGTGACTATC –(3'), anti-sense (5')– CAGAGCTGGTACTTTGGTGTTC –(3')	(Izquierdo et al., 2018)
qPCR <i>Tnfa</i> sense (5')– CCCTCACACTCAGATCATCTTCT –(3'), anti-sense (5')– GCTACGACGTGGGCTACAG –(3')	(Hernández-García et al., 2022)
qPCR <i>Ccl2</i> sense (5')– GTCCCTGTCATGCTTCTGG –(3'), anti-sense (5')– GCGTAACTGCATCTGGCT –(3')	This paper
qPCR <i>Abcg1</i> sense (5')– TGACACATCTGCGAATCAC –(3'), anti-sense (5')– AGGGGAAAGGTCAGAACG –(3')	This paper
qPCR <i>Pparg</i> sense (5')– GGAAGCACTCGCATTCCTT –(3'), anti-sense (5')– TCGCACTTTGGTATTCTTGGAG –(3')	This paper
qPCR <i>Ppara</i> sense (5')– ACAAGGCCTCAGGGTACCA –(3'), anti-sense (5')– GCCGAAAGAAGCCCTTACA –(3')	(Martínez-López et al., 2019)
qPCR <i>Pnpla2</i> sense (5')– TTCACCATCCGCTTGTGGAG –(3'), anti-sense (5')– AGATGGTCACCCAATTTCTC –(3')	This paper
qPCR <i>Lipe</i> sense (5')– TCCTCAGAGACCTCCGACTG –(3'), anti-sense (5')– ACACACTCCTGCGCATAGAC –(3')	This paper
qPCR <i>Hmgcs2</i> sense (5')– ATACCACCAACGCCTGTTATGG –(3'), anti-sense (5')– AATGTCACCACAGACCACCAG –(3')	This paper
qPCR <i>Hmgcl</i> sense (5')– ACTACCCAGTCCTGACTCCAA –(3'), anti-sense (5')– TAGAGCAGTTCGCGTTCTTCC –(3')	This paper
qPCR <i>Cebpa</i> sense (5')– CAAGAACAGCAACGAGTACCG –(3'), anti-sense (5')– GTCACTGGTCAACTCCAGCAC –(3')	This paper
qPCR <i>Fasn</i> sense (5')– AGAGATCCCAGACGCTTCT –(3'), anti-sense (5')– GCTTGGTCCTTTGAAGTCGAAGA –(3')	This paper
qPCR <i>Ppargc1a</i> sense (5')– TATGGAGTGACATAGAGTGTGCT –(3'), anti-sense (5')– CCACTTCAATCCACCCAGAAAG –(3')	(Matesanz et al., 2018)
qPCR <i>Uqcrcq</i> sense (5')– CCTACAGCTTGTCGCCCTTT –(3'), anti-sense (5')– GATCAGGTAGACCACTACAAACG –(3')	This paper
qPCR <i>Cox10</i> sense (5')– AGAAGAQGCTATACAGGGATTGCC –(3'), anti-sense (5')– CTGTGTGACATACATGCGCTT –(3')	This paper
qPCR <i>Atp5a1</i> sense (5')– CACAGCTGAGATGTCTCCA –(3'), anti-sense (5')– CATTGTCCGGTTCCAAGTTC –(3')	This paper
qPCR <i>Nos2</i> sense (5')– AATCTTGGAGCGAGTTGTGG –(3'), anti-sense (5')– CAGGAAGTAGGTGAGGGCTTG –(3')	This paper
qPCR <i>Cd80</i> sense (5')– CTGGGAAAACCCCCAGAAG –(3'), anti-sense (5')– TGACAACGATGACGACGACTG –(3')	This paper
qPCR <i>Il10</i> sense (5')– GCTCTTACTGACTGGCATGAG –(3'), anti-sense (5')– CGCAGCTCTAGGAGCATGTG –(3')	(Hernández-García et al., 2022)

qPCR <i>Stat6</i> sense (5')– CTCTGTGGGGCCTAATTTCCA –(3'), anti-sense (5')– CATCTGAACCGACCAGGAACT –(3')	This paper
qPCR <i>Tgfb1</i> sense (5')– GCAGTGGCTGAACCAAGGA –(3'), anti-sense (5')– AAAGAGCAGTGAGCGCTGAATC –(3')	(Martínez-López et al., 2019)
qPCR <i>Vegfa</i> sense (5')– AGTCCCATGAAGTGATCAAGTTCA –(3'), anti-sense (5')– ATCCGCATGATCTGCATGG –(3')	This paper
qPCR <i>Ifng</i> sense (5')– CTGCCACGGCACAGTCATTG –(3'), anti-sense (5')– TGCATCCTTTTTTCGCCTTGC –(3')	(Hernández-García et al., 2022)
qPCR <i>Il1b</i> sense (5')– CTGAACTCAACTGTGAAATGCCA –(3'), anti-sense (5')– AAAGGTTTGGGAAGCAGCCCT –(3')	(Hernández-García et al., 2022)
qPCR <i>Arg1</i> sense (5')– CTCCAAGCCAAAGTCCTTAGAG –(3'), anti-sense (5')– AGGAGCTGTCATTAGGGACATC –(3')	(Izquierdo et al., 2018)
qPCR <i>Mrc1</i> sense (5')– TGATTACGAGCAGTGGAAGC –(3'), anti-sense (5')– GTTCACCGTAAGCCCAATTT –(3')	(Rao et al., 2014)
qPCR <i>Clec10a</i> sense (5')– CTCTGGAGAGCACAGTGGAG –(3'), anti-sense (5')– ACTTCCGAGCCGTTGTTCT –(3')	(Rao et al., 2014)
qPCR <i>Retnla</i> sense (5')– CCAATCCAGCTAACTATCCCTCC –(3'), anti-sense (5')– ACCCAGTAGCAGTCATCCCA –(3')	(Rao et al., 2014)
qPCR <i>Siglecf</i> sense (5')– CTGGCTACGGACGGTTATTCG –(3'), anti-sense (5')– GGAATTGGGGTACTGGACTTG –(3')	(Rao et al., 2014)
qPCR <i>Il4</i> sense (5')– GGTCTCAACCCCAAGTAGT –(3'), anti-sense (5')– GCCGATGATCTCTCTCAAGTGAT –(3')	(Rao et al., 2014)
qPCR <i>Il13</i> sense (5')– CCTGGCTCTTGCTTGCCTT –(3'), anti-sense (5')– GGTCTTGTGTGATGTTGCTCA –(3')	(Rao et al., 2014)
qPCR <i>Ucp1</i> sense (5')– GTGAACCCGACAACCTTCCGAA –(3'), anti-sense (5')– TGCCAGGCAAGCTGAAACTC –(3')	(Rao et al., 2014)
qPCR <i>Cidea</i> sense (5')– TGCTCTTCTGTATCGCCAGT –(3'), anti-sense (5')– GCCGTGTTAAGGAATCTGCTG –(3')	(Rao et al., 2014)
qPCR <i>Dio2</i> sense (5')– CAGTGTGGTGCACGTCTCCAATC –(3'), anti-sense (5')– TGAACCAAAGTTGACCACCAG –(3')	(Rao et al., 2014)
qPCR <i>Prdm16</i> sense (5')– CAGCACGGTGAAGCCATTC –(3'), anti-sense (5')– GCGTGCATCCGCTTGTG –(3')	(Rao et al., 2014)
qPCR <i>Esrra</i> sense (5')– GCAGGGCAGTGGGAAGCTA –(3'), anti-sense (5')– CCTCTTGAAGAAGGCTTTGCA –(3')	(Rao et al., 2014)
qPCR <i>Xbp1</i> sense (5')– AAACAGAGTAGCAGCTCAGACTGC –(3'), anti-sense (5')– TCCTTCTGGGTAGACCTCTGGGA –(3')	(Han et al., 2009)
qPCR <i>18S rRNA</i> sense (5')– GTAACCCGTTGAACCCATT–(3'), anti-sense (5')– CCATCCAATCGGTAGTAGCG–(3')	This paper
qPCR <i>mt-Co2</i> sense (5')–CTACAAGACGCCACAT–(3'), anti-sense (5')–GAGGGGGAGAGCAAT–(3')	(Matesanz et al., 2018)
qPCR <i>Sdh</i> sense (5')–TACTACAGCCCAAGTCT–(3'), anti-sense (5')–TGGACCCATCTTCTATGC–(3')	(Matesanz et al., 2018)

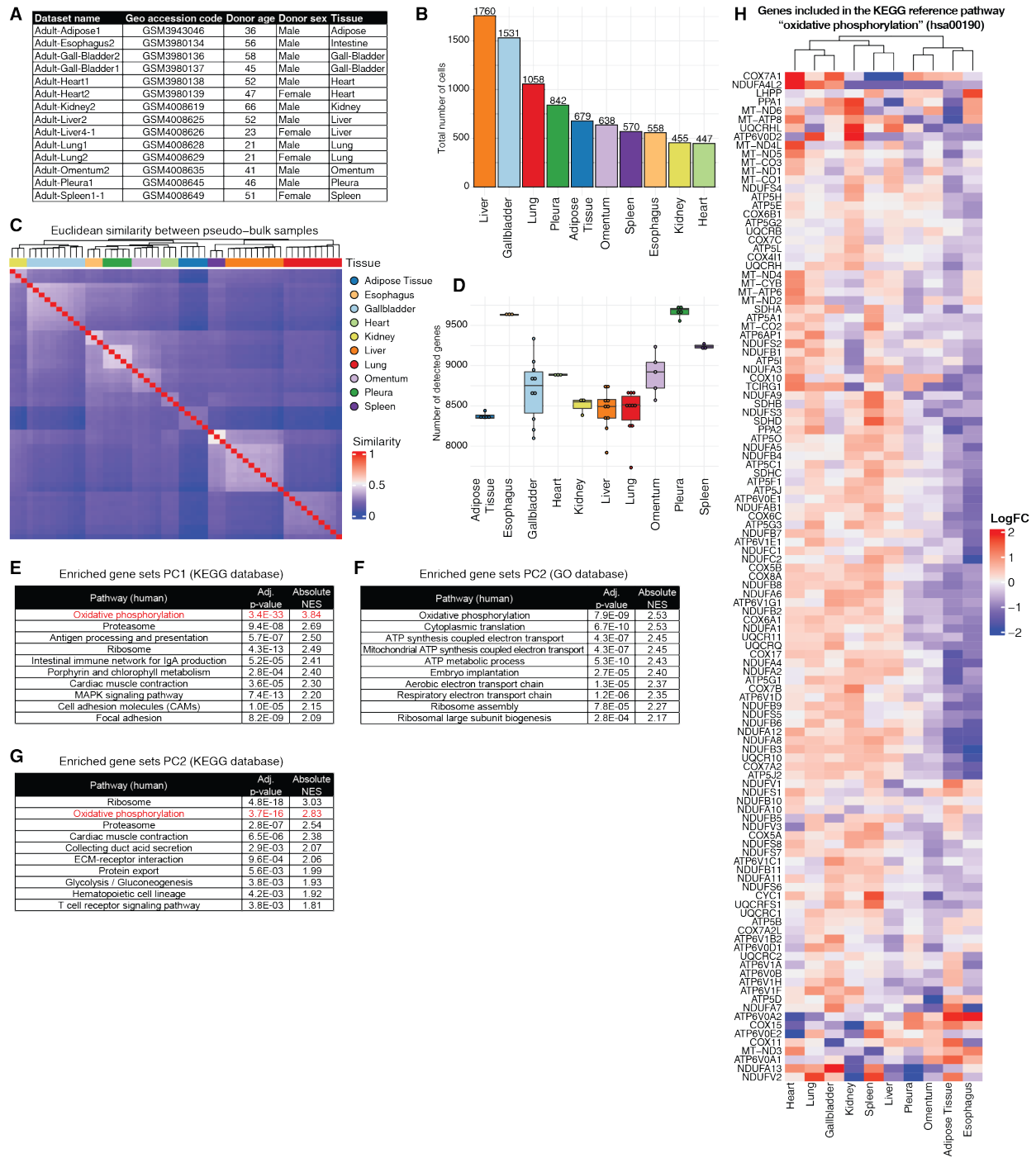


Figure S1. Related to Figure 1.

(A) List of publicly available scRNAseq datasets with donor information from the Human Cell Landscape (<https://db.cngb.org/HCL/>) that were used for the analysis of human TMF clusters shown in Figure 1A.

(B) Number of human TMF cells from each tissue used to build pseudo-bulk samples.

(C) Heatmap of samples clustered using hierarchical clustering based on Euclidean distances transformed into similarities and the complete agglomeration method of each pseudo-bulk sample of human TMF cells.

(D) Boxplots of number of detected genes per pseudo-bulk sample. Human TMF pseudo-bulk samples were built controlling for the number of detected genes per sample in order to avoid possible biases in further analysis. Ranges are within 7734 and 9733 genes.

(E to G) Pre-ranked enrichment analysis of the genes defining PC1 (E) or PC2 (F and G) of human TMFs in the reference pathways of the KEGG database (<https://www.genome.jp/kegg/pathway.html>) (E and G) or in the biological processes of the GO resource (<http://geneontology.org/>) (F). NES, normalized enrichment score; Adj., adjusted with Benjamini–Hochberg correction.

(H) Heat map of log-Fold change (FC) of all genes included in the KEGG reference pathway “oxidative phosphorylation” (hsa00190) in the TMF clusters identified in the human scRNAseq data analysis calculated comparing each individual tissue with the mean of all tissues. Genes (rows) and samples (columns) are ordered using hierarchical clustering of log-Fold changes and the complete agglomeration method.

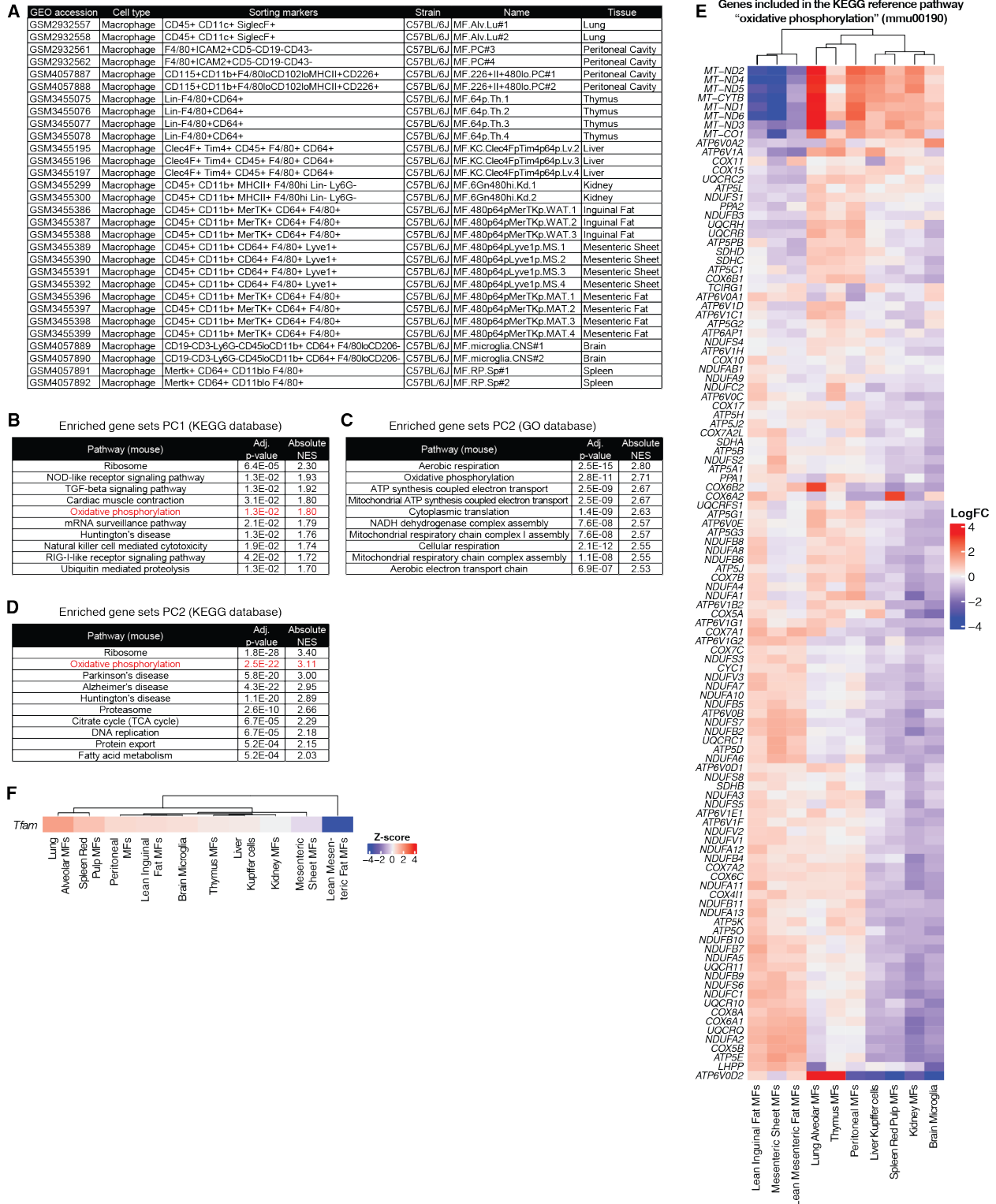


Figure S2. Related to Figure 1.

(A) List of publicly available RNAseq data from the Immunological Genome Project (<https://www.immgen.org/ImmGenpubs.html>) that were used for the analysis of mouse TMF populations shown in Figure 1C-1E.

(B to D) Pre-ranked enrichment analysis of the genes defining PC1 (B) or PC2 (C and D) of mouse TMFs in the reference pathways of the KEGG database (B and D) or in the biological processes of the GO resource (C). NES, normalized enrichment score; Adj., adjusted with Benjamini–Hochberg correction.

(E and F) Heat map of log-Fold change (FC) of all genes included in the KEGG reference pathway “oxidative phosphorylation” (mmu00190) (E) and heatmap of Z score of *Tfam* (F) in the mouse TMF population RNAseq data analysis calculated comparing each individual tissue with the mean of all tissues. Genes (rows) and samples (columns) are ordered using hierarchical clustering of log-Fold changes and the complete agglomeration method.

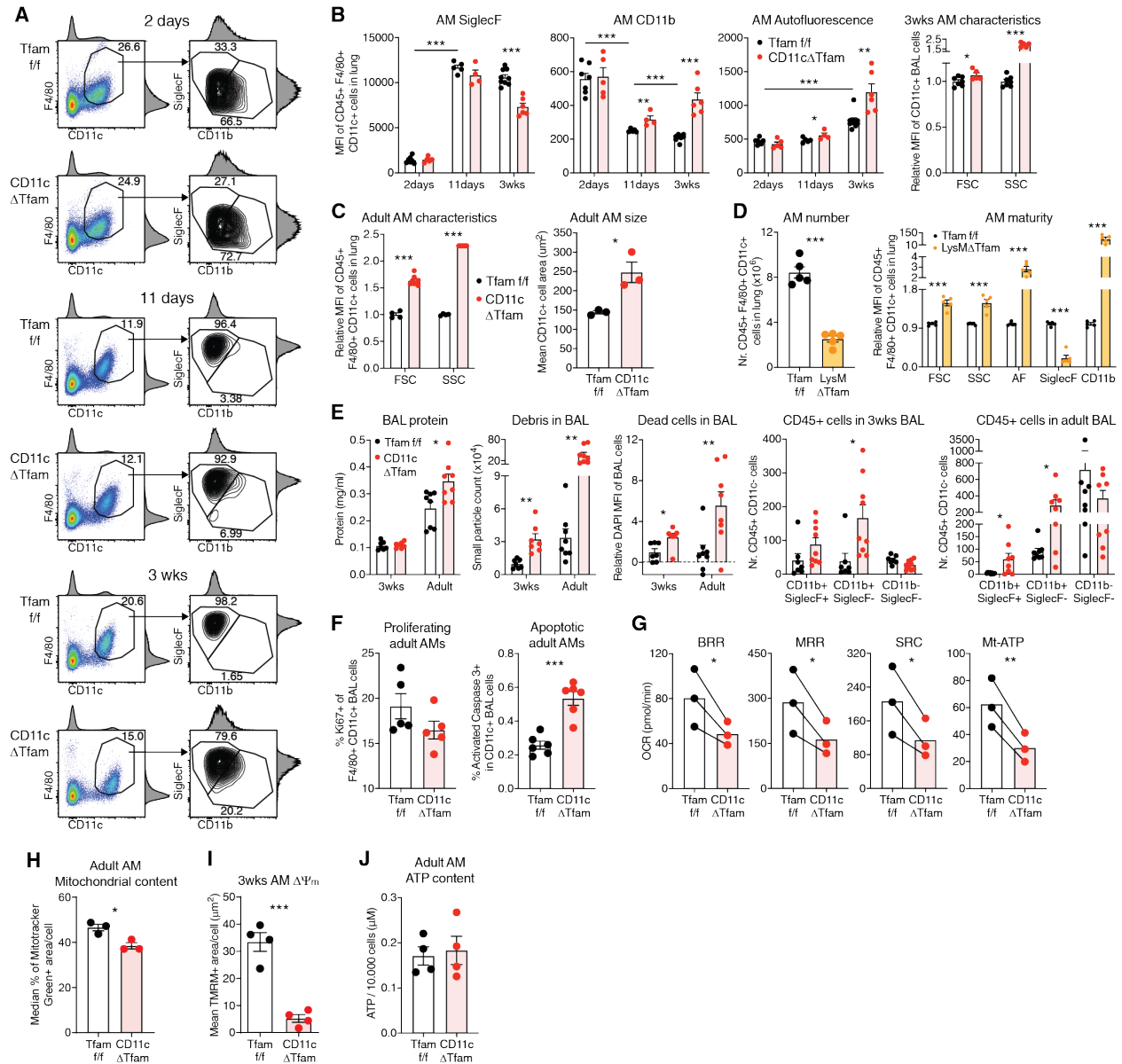


Figure S3. Related to Figure 3.

2 day-old, 11 day-old, 3 week (wks)-old or adult (6-8 week-old) mice or their AMs in the lung were analyzed.

(A and B) Representative plots (A, gated on CD45⁺ lung cells) and (relative) median fluorescence intensity (MFI) of autofluorescence, Siglec F, CD11b, FSC or SSC (B) of CD45⁺ F4/80⁺ CD11c⁺ cells in the lung or CD11c⁺ cells in the BAL of *Tfam*^{*f/f*} and *CD11c* Δ *Tfam* mice at various ages (n=4-9).

(C) Relative MFI of FSC or SSC of CD45⁺ F4/80⁺ CD11c⁺ cells in the lung (left, n=4-8) and cell size determined by fluorescence microscopy of CD11c⁺ cells from BAL of adult *Tfam*^{*f/f*} and *CD11c* Δ *Tfam* mice (right, n=3 [mean of 54-231 cells/mouse]).

(D) Flow cytometric quantification of numbers (left) and relative MFI of FSC, SSC, autofluorescence (AF), Siglec F or CD11b (right) of CD45⁺ F4/80⁺ CD11c⁺ cells in the lung of adult *Tfam*^{*f/f*} and *LysM* Δ *Tfam* mice (n=5).

(E) Analysis of BAL of 3 week-old or adult *Tfam*^{*f/f*} and *CD11c* Δ *Tfam* mice for protein levels, amount of debris, levels of dead DAPI⁺ cells and number of CD45⁺ CD11c⁻ CD11b⁺ or- Siglec F⁺ or- cells (n=7-9).

(F) Flow cytometric quantification and representative plots of frequency of Ki67⁺ (n=5, left) or activated caspase 3⁺ cells (n=6, right) in (F4/80⁺) CD11c⁺ cells in BAL of adult *Tfam*^{fl/fl} and *CD11cΔTfam* mice.

(G) Basal respiratory rate (BRR), maximal respiratory rate (MRR), spare respiratory capacity (SRC) and respiration linked to mitochondrial ATP (mt-ATP) production of CD11c⁺ cells from BAL of adult *Tfam*^{fl/fl} and *CD11cΔTfam* mice (n=3 merged from 5-10 mice).

(H) Quantification of mitochondrial content by fluorescence microscopy of MitoTracker Green staining of CD11c⁺ cells from BAL of adult *Tfam*^{fl/fl} and *CD11cΔTfam* mice (n=3 [mean of 54-231 cells/mouse]).

(I) Quantification of mitochondrial membrane potential ($\Delta\Psi_m$) by fluorescence microscopy of Tetramethylrhodamine methyl ester (TMRM) staining of CD11c⁺ cells from BAL of 3 week-old *Tfam*^{fl/fl} and *CD11cΔTfam* mice (n=4 [mean of 9-85 cells/mouse]).

(J) ATP levels in F4/80⁺ CD11c⁺ cells from the BALs of adult mice (n=4).

Data are merged from at least 2 independent experiments and presented as mean \pm SEM. Dots represent individual data points. Statistical analysis by unpaired (B-F, H-J) or paired (G) Student's t-test. *p \leq 0.05, **p \leq 0.01, ***p \leq 0.001.

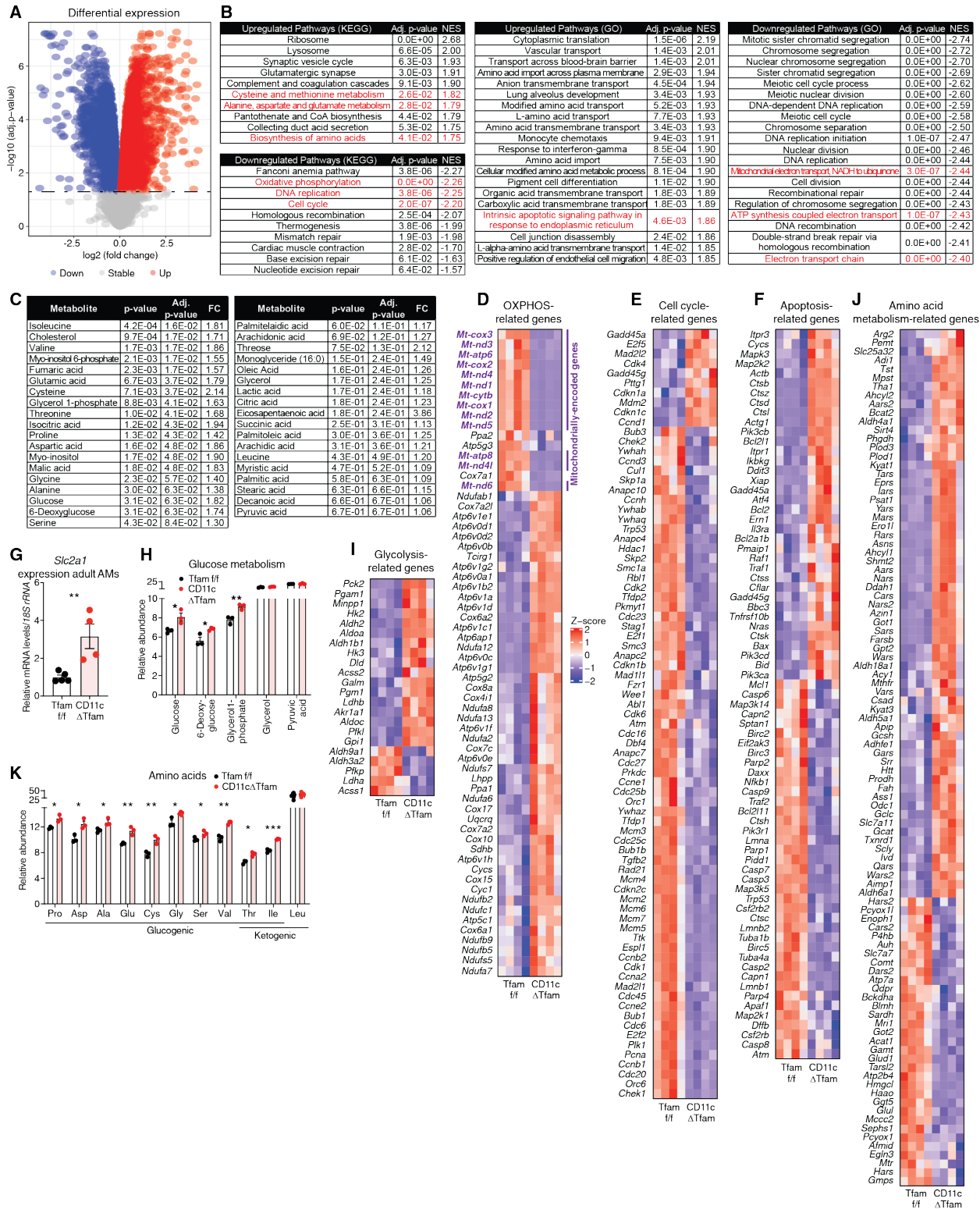


Figure S4. Related to Figure 3.

AMs from *Tfam^{f/f}* and *CD11cΔTfam* mice were analyzed.

(A) Volcano plot of deregulated genes detected in RNAseq of FACS-sorted CD45⁺ F4/80⁺ CD11c⁺ lung cells from 3 week-old mice (n=4).

(B) Pre-ranked enrichment analysis of deregulated genes in the analysis shown in (A) in pathways of the KEGG database (left) or the GO resource (center and right). NES, normalized enrichment score *CD11cΔTfam* mice vs *Tfam*^{ff} AMs; Adj., adjusted with Benjamini–Hochberg correction.

(C) Overview of metabolites detected by untargeted GC/MS analysis of FACS-sorted F4/80⁺ CD11c⁺ cells from BAL of adult mice (n=3 merged from 13-30 mice). FC, fold-change *CD11cΔTfam* mice vs *Tfam*^{ff} AMs.

(D to F) Heat map of expression levels of deregulated (Adj. p-value <0.05) OXPHOS-related (KEGG reference pathway mmu00190, D), cell cycle-related (KEGG mmu04110, E) and apoptosis-related (KEGG mmu04210, F) genes detected in the RNAseq of FACS-sorted CD45⁺ F4/80⁺ CD11c⁺ lung cells from 3 week-old mice shown in (A).

(G) *Slc2a1* mRNA levels in FACS-sorted F4/80⁺ CD11c⁺ lung cells from adult mice (n=4-5).

(H) Relative abundance of the indicated glucose metabolism intermediates detected by the GC/MS analysis of FACS-sorted F4/80⁺ CD11c⁺ cells from BAL of adult mice (n=3 merged from 13-30 mice) shown in (C).

(I and J) Heat map of expression levels of deregulated (Adj. p-value <0.05) glycolysis-related (KEGG mmu00010, I) and amino acid metabolism-related (GO reference pathway 0006520, J) genes detected in the RNAseq of FACS-sorted CD45⁺ F4/80⁺ CD11c⁺ lung cells from 3 week-old mice shown in (A).

(K) Relative abundance of the indicated amino acids detected by the GC/MS analysis of FACS-sorted F4/80⁺ CD11c⁺ cells from BAL of adult mice (n=3 merged from 13-30 mice) shown in (C).

Data are merged from at least 2 independent experiments and presented as mean ± SEM. Dots represent individual data points. Statistical analysis by unpaired (G-K) with Benjamini–Hochberg correction (C) Student's t-test. *p≤0.05, **p≤0.01, ***p≤0.001.

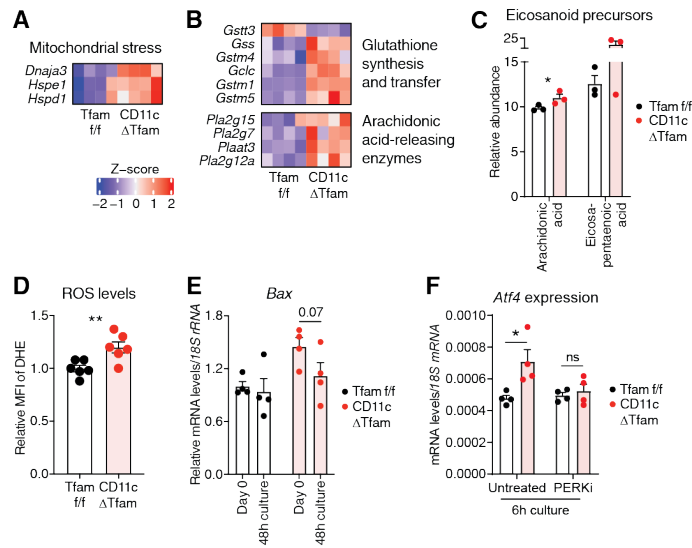


Figure S5. Related to Figure 4.

Tfam^{f/f} and *CD11c* Δ *Tfam* mice or their AMs in the lung were analyzed.

(A and B) Heat map of expression levels of selected mitochondrial stress-related genes (A) and glutathione synthesis and transfer-related genes (B, top) and genes encoding arachidonic acid-releasing enzymes (B, bottom) detected in the RNAseq of FACS-sorted CD45⁺ F4/80⁺ CD11c⁺ lung cells from 3 week-old mice shown in Figure S4A.

(C) Relative abundance of eicosanoid precursors detected in the GC/MS analysis of FACS-sorted F4/80⁺ CD11c⁺ cells from BALs of adult mice (n=3 merged from 13-30 mice) shown in Figure S4C.

(D) Flow cytometric quantification of relative MFI of dihydroethidium (DHE, n=6) of F4/80⁺ CD11c⁺ lung cells from 3 week-old mice.

(E) CD11c⁺ cells were magnetically purified from BALs of 3 week-old mice and either directly analyzed (Day 0) or cultured for 48h before analysis of *Bax* mRNA levels (n=4 merged from 2-4 mice).

(F) CD11c⁺ cells were magnetically purified from BALs of adult mice and cultured for 6h under presence or not of 1 μ M PERK inhibitor GSK2606414 before analysis of *Atf4* mRNA levels (n=4 merged from 3-4 mice).

Data are merged from at least 2 independent experiments and presented as mean \pm SEM. Dots represent individual data points. Statistical analysis by unpaired Student's t-test. *p \leq 0.05, ns not significant.

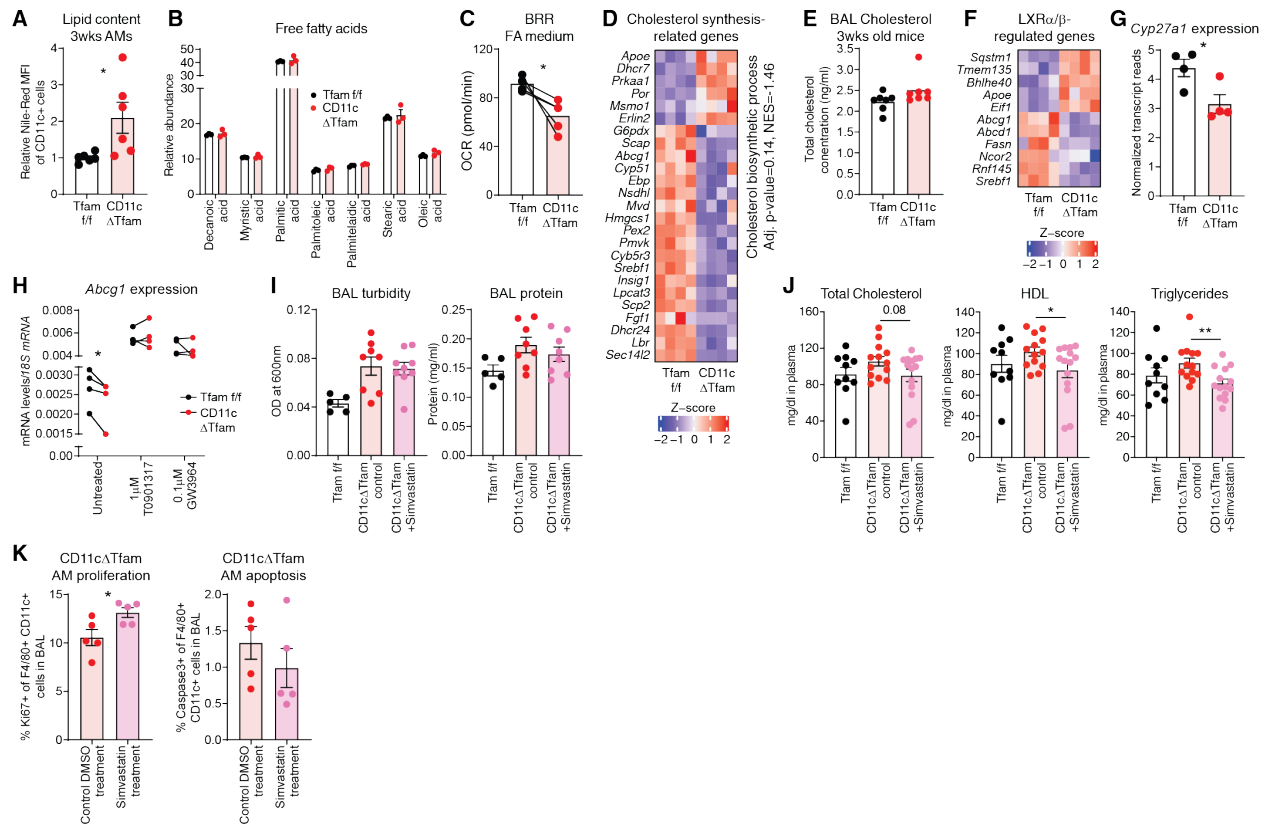


Figure S6. Related to Figure 5.

Tfam^{ff} and *CD11c* Δ *Tfam* mice or their AMs in the lung were analyzed.

(A) Flow cytometric quantification of relative MFI of Nile-Red staining of CD11c⁺ cells from BAL of 3 week-old mice (n=6).

(B) Relative abundance of free FAs detected in the GC/MS analysis of FACS-sorted F4/80⁺ CD11c⁺ cells from BALs of adult mice (n=3 merged from 13-30 mice) shown in Figure S4C.

(C) Basal respiratory rate (BRR) of CD11c⁺ cells from BAL of adult *Tfam*^{ff} and *CD11c* Δ *Tfam* mice in media containing 5mM L-carnitine and 50 μ M palmitoyl-CoA (n=4 merged from 5-10 mice).

(D) Heat map of expression levels of deregulated genes included in the “cholesterol biosynthetic process” (GO process GO:0006695) detected in the RNAseq of CD45⁺ F4/80⁺ CD11c⁺ lung cells from 3 week-old mice.

(E) Quantification of total cholesterol levels in BAL of 3 week-old mice (n=7).

(F and G) Heat map of expression levels of deregulated genes controlled by LXR α / β (as determined on the DoRoThEA database [https://dorothea.opentargets.io], F) and expression of *Cyp27a1* (G) detected in the RNAseq of CD45⁺ F4/80⁺ CD11c⁺ lung cells from 3 week-old mice.

(H) CD11c⁺ cells were magnetically purified from BALs of adult mice and cultured for 24h under presence or not of LXR agonists 1 μ M T0901317 or 0.1 μ M GW3965 before analysis of *Abcg1* mRNA levels (n=4 merged from 4-5 mice).

(I and J) Turbidity and protein levels in BAL (I) and well as levels of total cholesterol, HDL and triglycerides in plasma (J) of mice treated with Simvastatin or control DMSO for 8 weeks (n=5-13).

(K) Flow cytometric quantification of frequency of Ki67⁺ (left) or activated caspase 3⁺ cells (right) in F4/80⁺ CD11c⁺ cells in BAL of mice treated with Simvastatin or control DMSO for 3 weeks (n=5).

Data are merged from at least 2 independent experiments and presented as mean \pm SEM. Dots represent individual data points. Statistical analysis by unpaired (A, G, J and K) or paired (C and H) Student’s t-test.

*p \leq 0.05, **p \leq 0.01.

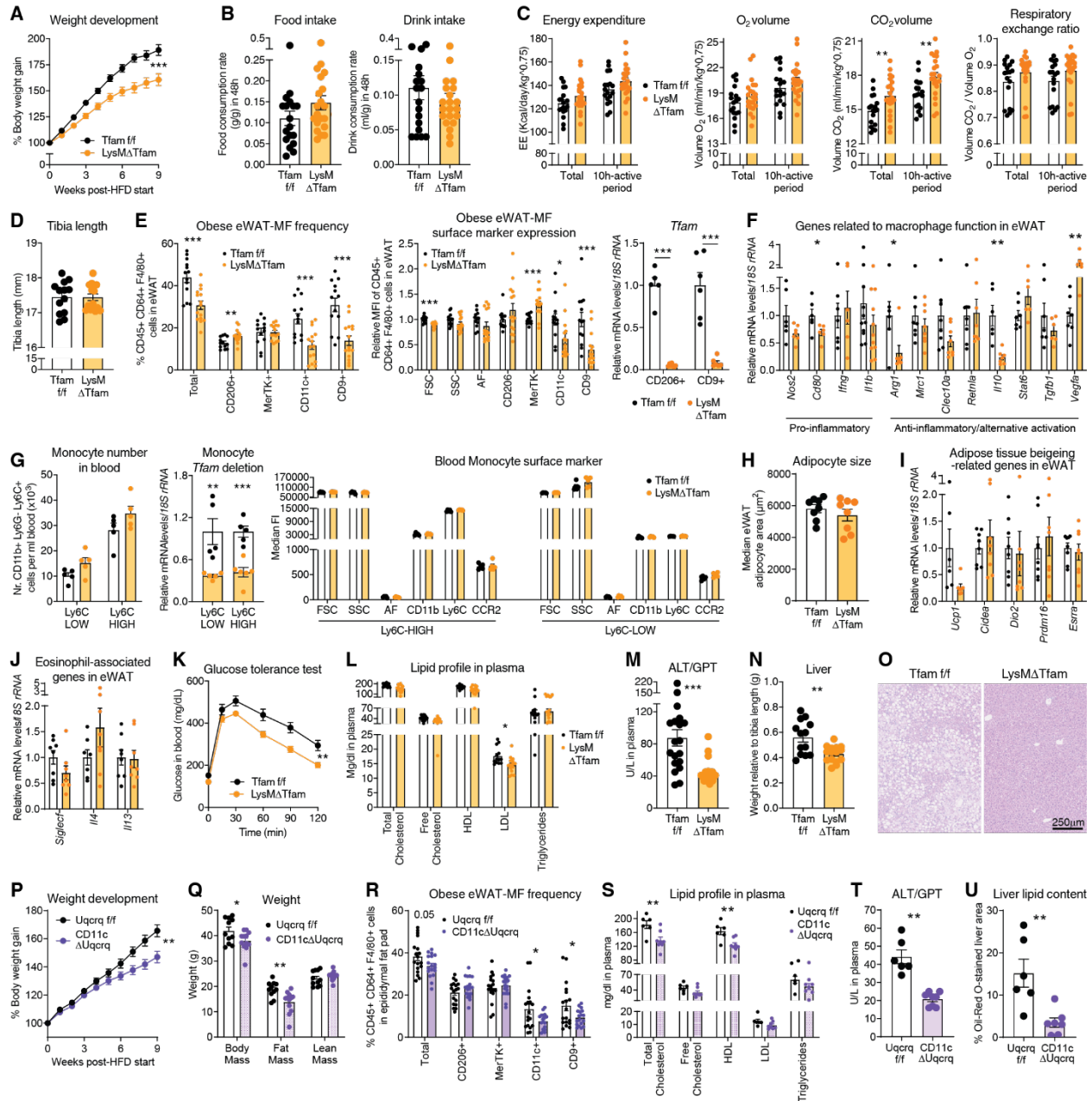


Figure S7. Related to Figure 7.

Tfam^{fl/fl} and *LysM Δ Tfam* or *Uqcrcq^{fl/fl}* and *CD11c Δ Uqcrcq* mice were fed an HFD for 9 weeks and analyzed.

(A) Weight development over time on HFD diet start at week 0 (n=13-15).

(B) Food and drink intake of obese mice measured in metabolic cages (n=18-21).

(C) Energy expenditure, consumed O₂ volume, released CO₂ volume and calculated respiratory exchange ratio of obese mice measured in metabolic cages (n=18-22).

(D) Tibia length (n=13-15).

(E) Flow cytometric quantification of frequencies of CD45⁺ CD64⁺ F4/80⁺ cells or cells that also express the indicated surface markers in alive cells from eWAT of obese mice (left, n=13-15). Relative median fluorescence intensity (MFI) of indicated parameters or markers on CD45⁺ CD64⁺ F4/80⁺ cells from eWAT

of obese mice (center, n=13-15). *Tfam* mRNA levels in FACS-sorted CD45⁺ CD64⁺ F4/80⁺ and CD206⁺ or CD9⁺ cells from eWAT of obese mice (right, n=5-7).

(F) mRNA levels of selected genes associated with macrophage functions in eWAT (n=6-11).

(G) Flow cytometric quantification of numbers (top left) and MFI of indicated parameters or markers (bottom) on CD11b⁺ Ly6G⁻ and Ly6C^{low} or Ly6C^{high} cells in blood of lean mice before start of HFD treatment (n=5). *Tfam* mRNA levels in FACS-sorted CD11b⁺ Ly6G⁻ and Ly6C^{low} or Ly6C^{high} cells from blood of lean mice (top right, n=5-6).

(H) Adipocyte size in obese eWAT measured by microscopy (n=9).

(I and J) mRNA levels of selected genes associated with adipose tissue beigeing (I) and eosinophil presence or function (J) in eWAT (n=6-8).

(K) Glucose levels over time in blood after intraperitoneal injection (time = 0) of glucose (n=13-16).

(L) Levels of total cholesterol, free cholesterol, HDL, LDL and triglycerides in plasma of HFD-fed mice (n=13-15).

(M) Alanine transaminase (ALT/GPT) levels in plasma (n=19-22).

(N) Weight of median lobe of livers from obese mice relative to tibia length (n=13-15).

(O) Representative image of eosin (pink) and hematoxylin (blue)-stained liver sections (scale bar: 250µm).

(P) Weight development over time on HFD diet start at week 0 (n=18-19).

(Q) Quantification of magnetic resonance imaging to determine body mass (n=11).

(R) Flow cytometric quantification of frequencies of CD45⁺ CD64⁺ F4/80⁺ cells or cells that also express the indicated surface markers in alive cells from eWAT of obese mice (n=18).

(S) Levels of total cholesterol, free cholesterol, HDL, LDL and triglycerides in plasma of HFD-fed mice (n=6-8).

(T) Alanine transaminase (ALT/GPT) levels in plasma (n=6-7).

(U) Quantification of Oil-Red O-stained liver sections (n=6-7).

Data are merged from at least 2 independent experiments and presented as mean ± SEM. Dots represent individual data points. Statistical analysis by two-way ANOVA with Geisser-Greenhouse correction (A, K and P) or unpaired Student's t-test (B-J, L-N and Q-U). *p≤0.05, **p≤0.01, ***p≤0.001.